Numerical Investigation of the Campbell Diffuser Concept

by

Wai Chung AU

B.A., Cambridge University (1988)

SUBMITTED IN PARTIAL FULFILLMENT OF THE
REQUIREMENTS FOR THE DEGREE OF

Master of Science
in
Aeronautics and Astronautics
at the
Massachusetts Institute of Technology

February, 1991

Signature of Author ____________________
Department of Aeronautics and Astronautics
December 18, 1990

Certified by ____________________
Dr. Choon S. Tan
Thesis Supervisor

Accepted by ____________________
Professor Harold Y. Wachman
Chairman, Department Graduate Committee

Numerical Investigation of the Campbell Diffuser Concept

by

Wai Chung AU

Submitted to the Department of Aeronautics and Astronautics
on December 18, 1990, in partial fulfillment of the
requirements for the degree of
Master of Science

Abstract

Campbell diffusers have a unique feature in that they lack axial symmetry in the end walls. It has been proposed that the asymmetry of the end wall in a vaned diffuser can be tailored to improve its performance. This concept is applied to the redesign of two vaned diffuser configurations: (1) diffuser with straight leading edge; (2) diffuser with parabolic leading edge. In the redesign, the original axisymmetric end wall configuration is modified so that the resulting end walls on the pressure side converge from the leading edge to the throat and then diverge back to the original passage depth. Thus to maintain the same flow area distribution as the original vaned diffuser, the end walls on the suction side would have to be tailored so that they diverge from the beginning of the channel region to the throat before converging back to the original passage depth at the exit. A three dimensional inviscid Euler code is used to evaluate the performance of these diffusers. The performance of Campbell diffusers and two dimensional diffusers have been compared at an optimized operating point. The operating point has been chosen such that the Mach number at the throat is as high as possible (with a limit of one). Important parameters that govern the extent of the flow response to end walls changes are studied. These are (i) the pitch-chord ratio; and (ii) the ratio of passage depth to chord. When these two ratios are small (of the order of 0.1), which is typically found in practical vaned diffusers, the flow is essentially one dimensional so that its response to the end wall contouring is not as dramatic. However, when either of the two ratios is large enough, the effect of end wall contouring can be more significant. In the case where the passage depth to chord ratio is sufficiently large, Campbell diffusers can potentially outperform two-dimensional diffusers in term of pressure recovery based on the present computational results.

Thesis Supervisor: Dr. Choon S. Tan
Title: Principal Research Engineer

Acknowledgements

I would like to take this opportunity to thank all the people helping in this research project. First of all, thanks are given to my supervisor, Dr. Choon Tan, for his time and patience. To Prof. Edward Greitzer, for his brief supervision when Dr. Tan was away. I am grateful to Dr. Belgacem Jery for his personal support throughout the project. Prof. Nick Cumpsty deserves special thanks for his enlightening ideas.

This research project would not be possible without the help of many people in NASA Lewis research center. I wish to express my thank to Dr. John Adamczyk for letting me use his code for the research. I am indebted to Dr. Kevin Kirtley for his time spent in instructing me in the use of the computer code and helping me in debugging. I am grateful to Mr. Tim Beach for his aid in generating computational grids at the early stage of the research.

I am grateful to my friends and colleagues for providing support and outlets for complaining. I would like express my gratitude to my old friend Norman Lee for his help in solving many of my problems; technical as well as personal ones. Thanks go to Alex Fung for his enthusiasm in problem solving. To my officemates Dave, Eric, Laurent and Seung Jin, who create fun in the office. To my friend Ka Shun Wong, who has helped me since I arrived in Boston.

I am truly grateful to the support I have received from my family. Thanks Mum, Dad, Virginia, Fredrick and Wilfred. Your unfailing love is the reason for my survival in MIT.

This work was supported by NASA Lewis Research Center grant NAG 3-1028 with Dr. Arthur Wennerstrom of AFAWL and Mr. Larry Schumann of Army Propulsion Directorate as technical monitors.

Nomenclature

A	flow area (normal to mean velocity vector)
AR	aspect ratio
a	speed of sound
CFL	Courant-Friedrichs-Lewy number
c	diffuser chord length
c_P	pressure recovery coefficient
D	dissipation operator
e_0	total internal energy/unit mass
h	static enthalpy/unit mass
h_0	total enthalpy/unit mass
J_-, J_+	Riemann invariants
LE	leading edge
M	Mach number
MR_2	mach number ratio $= M_{rel1t}/M_{rel2j}$
MS	midstream
$\dot{m}$	mass flow rate
N	shaft speed
$\hat{n}$	unit vector normal to boundary
P	static pressure
PS	pressure side
P_0	stagnation pressure
pr	pressure ratio
r	radius
s	entropy,distance along streamline
SS	suction side
t	time
T	static temperature

TE	trailing edge
T_0	stagnation temperature
v_r	radial velocity
v_θ	tangential velocity
v_z	axial velocity
V	volume of computational cell
Z	number of vanes
α	absolute flow angle
$\alpha_1, \alpha_2, \alpha_3, \alpha_4$	multistage timestepping coefficients
β	swirl angle
δ	central difference operator,diffuser passage depth
Δt	time step size
ϵ	diffuser passage width
$\epsilon^{(2)}, \epsilon^{(4)}$	second and fourth difference artifical viscosity coefficients
γ	ratio os specific heats
2θ	diffuser divergence angle
ρ	density
ρ_0	stagnation density
ψ	streamfunction

subscripts

0	stagnation
1,2,··	station
D	diffuser
j	jet

r	radial component
rel	relative to impeller coordinates
t	tip
z	axial component
θ	tangential component

superscripts

‾	mass average quantity $(\int x\rho\, dV)/(\int \rho\, dV)$
^	dimensional quantity
*	nondimensionalized quantity
n	quantity at n^{th} iteration

station

1	impeller inlet
2	impeller exit
3	diffuser inlet
4	diffuser exit

Contents

List of Figures

List of Tables

Chapter 1

Introduction

1.1 Introduction

Small gas turbine engines utilizing centrifugal compressor stages are used as helicopter engines and are increasingly tested for automobiles applications. Currently, impeller efficiencies are of the order of 90%. However, the stage efficiency is lower than that due to the diffuser performance. Both the efficiency and surge-to-choke operating range of a centrifugal compressor depend strongly on the performance of the diffuser. Figure 1-1(from [1]) illustrates the importance of diffuser performance to the stage. It shows the effect of impeller diffusion (expressed by the diffusion parameter,MR_2) and of diffuser recovery (C_{pD}) on stage efficiency. The improvements in stage efficiency with diffuser recovery are quite uniform with about 3 point increase in C_{pD} giving a point increase in stage efficiency. High diffuser performance cannot be easily obtained, especially in high pressure ratio designs [2]. This is because high pressure ratio compressors require vaned diffusers to achieve high pressure recovery and it is complicated to model the flow of the vaned diffuser theoretically or to investigate experimentally. The nonuniform flow at the impeller exit is viewed as unsteady flow by the diffuser vanes, while the presence of the diffuser vanes is seen as an unsteady disturbance by the impeller. It is not possible to choose a frame of reference which will produce only steady processes.

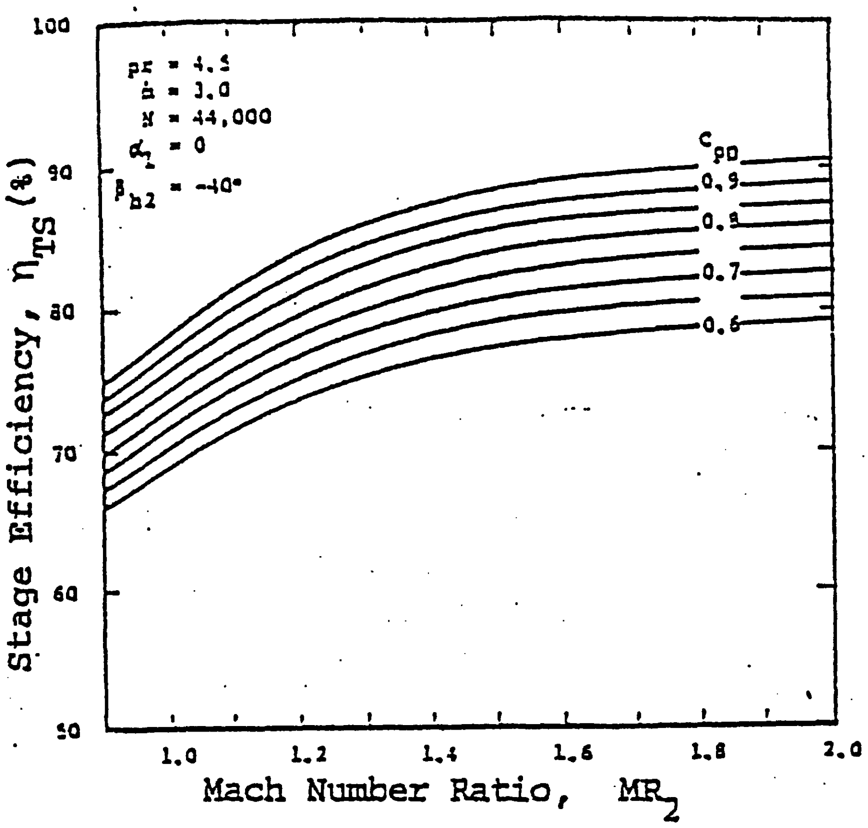

Figure 1-1: The influence of impeller and diffuser recovery performance upon stage efficiency

A way to improve the centrifugal compressor performance is to increase the speed of the impeller. The kinetic energy at the impeller exit will become so large that vane-less less diffusers are no longer suitable for efficient pressure recovery [3]. The geometrical constraint limits the size of the vaneless diffuser while a large radius of the vaneless diffuser is required to achieve efficient pressure recovery. Moreover, the high swirl flow due to high impeller speed will cause instability in vaneless diffusers and reverse flow will occur [4, 5]. Therefore these compressors have to be equipped with vaned diffusers. At a certain limit of impeller speed, the flow will become supersonic. By introducing a vaned diffuser in the supersonic region, shock waves may occur at the diffuser entrance region. The characteristic features of the flow field will be changed quite significantly. The shock wave can interact with the boundary layer, which may then separate. The influence of changes in diffuser geometry on the performance must be well understood before a systematic increase in the efficiency for a centrifugal compressor can be made. Vaned diffusers are most suitable for medium to high pressure ratio applications; they have been investigated experimentally and theoretically. Baghdadi and McDonald [6] used vortex nozzle to produce a wake-free, swirling, supersonic flow at the inlet to a radial diffuser. Visual studies and performance measurements had been made for three set of vane representing common designs for vaned diffusers. It was observed that the surge is an instability triggered by flow separation in the vaneless or semi-vaneless space ahead of the diffuser throat. The surge-to-choke operating range of the three vaned diffusers were found to be a function of the number of diffuser vanes only. Rayan and Yang [7] reported tests of vane-island diffusers at high swirl. Their study indicated that the performance of the vane-island diffuser depends on the fluid mechanics of the flow at the impeller exit. The investigation also showed that the radial distance from the vane leading edge to the impeller exit is one important factor in diffuser effectiveness. The minimum loss coefficient they could obtain was achieved when the vane-island leading edge was at a radius approximately equal to 1.2 time the diffuser inlet radius. Inoue and Cumpsty [8] presented experimental study of centrifugal impeller discharge flow in vaneless and vaned diffusers. They observed that the circumferential distortion from the impeller was attenuated very rapidly and had only minor effects on the flow inside the vaned diffuser passage. The effect of the diffuser vanes on the flow discharged from the impeller was evident and reversal of the flow back into the impeller was detected when the diffuser vanes were close to the impeller and the flow rate was not very high. On the other hand, Teipel,Weidermann,Jeske and Colantuoni [9, 10, 11, 12] have carried out in theoretical study of transonic radial vaned diffusers. Teipel and Wiedermann considered the influence of different geometries of the blades on the pressure distribution in transonic flow field. They changed the stagger angle of the diffuser vanes and observed that with increasing stagger angle change, the flow reacted very sensitively to altered pressure conditions at the diffuser exit. Colantuoni used a two-dimensional Euler code to study the effect of blade shape of transonic vaned diffusers on performance and range. He then optimized the blade shape to give a shock-free deceleration for the diffuser.

1.2 Background

The fluid dynamic task of diffusers is the conversion of kinetic energy into static pressure. In order to get an efficient stage, the kinetic energy must be efficiently recovered. Diffusers convert kinetic energy into static pressure through the principles of (i) conservation of mass and (ii) conservation of angular momentum.

i) conservation of mass:

an increase in flow area in order to bring about a reduction in the average velocity and hence an increase in static pressure.

ii) conservation of angular momentum:

a change in mean flow path radius to bring about a change in tangential velocity through, $rV_\theta \approx$ constant.

As mentioned in the previous section, vaned diffusers are used to increase the flow area to get sufficient pressure recovery. However, a good design is required to avoid high loss due to separation and to maintain stable operating conditions.

In 1978 Kenneth Campbell [13] proposed a centrifugal compressor diffuser which incorporated vanes and non-axisymmetric end walls. The unique feature of his design was the lack of axial symmetry in the end walls which was introduced in such a manner as to cause the flow to naturally follow the direction of the suction surface of the vane, thus reducing the vane-to-vane pressure gradient. His concept was proposed for subsonic diffusers and it was not quite successful [14]. However, in transonic and supersonic flow field, the flow is more sensitive to geometrical change than that in incompressible flow. His approach may have something to offer for supersonic diffusers which typically suffer from a strong inlet shock wave and the accompanying separation and high losses. Campbell's design approach may produce lower losses at the diffuser entrance.

1.3 Typical performance characteristics

Fig.1-2 and fig.1-3 (from [15]) show the typical performance characteristic for centrifugal compressors with and without vaned diffuser. The most noticeable difference between the characteristic maps is the much larger flow range exhibited by the vaneless configuration. However, the peak stage efficiency is 5 points higher for the vaned configuration. The speed lines tend to be steeper for the vaned configuration. All these differences are well known and expected.

1.4 Objectives

The objective of this investigation is to evaluate the potential merits of the Campbell design concept for diffusers of centrifugal compressors with supersonic flow at the impeller exit.

For a vane diffuser, Dean [2] divided the flow field into three regions (fig. 1-4). They are the vaneless region(I), semi-vaneless region(II) and the divergent channel(III). His flow model is based on the jet-wake flow pattern at the impeller exit. The flow pattern in regions (I) and (II) can be predicted with reasonable accuracy using his analytical results. He reported that optimization of the performance of a vaned diffuser depends on the interaction between impeller and diffuser (region (I)), interaction between the flow in the vaneless space and the leading edges of the diffuser (region (II)) as well as the region of the vaned diffuser (region (III)). Changing the passage width only alters the divergent channel geometry. However, it may affect the pressure distribution in other regions as well. The pressure distribution in turn has an influence on the shock. The criterion for judging the diffuser performance will be the strength of the shock and the overall pressure recovery. The strength of the shock is estimated from the Mach number distribution. The overall pressure recovery is given below:

$$c_{pD} = \frac{\bar{P}_4 - \bar{P}_2}{\bar{P}_{02} - \bar{P}_2}$$

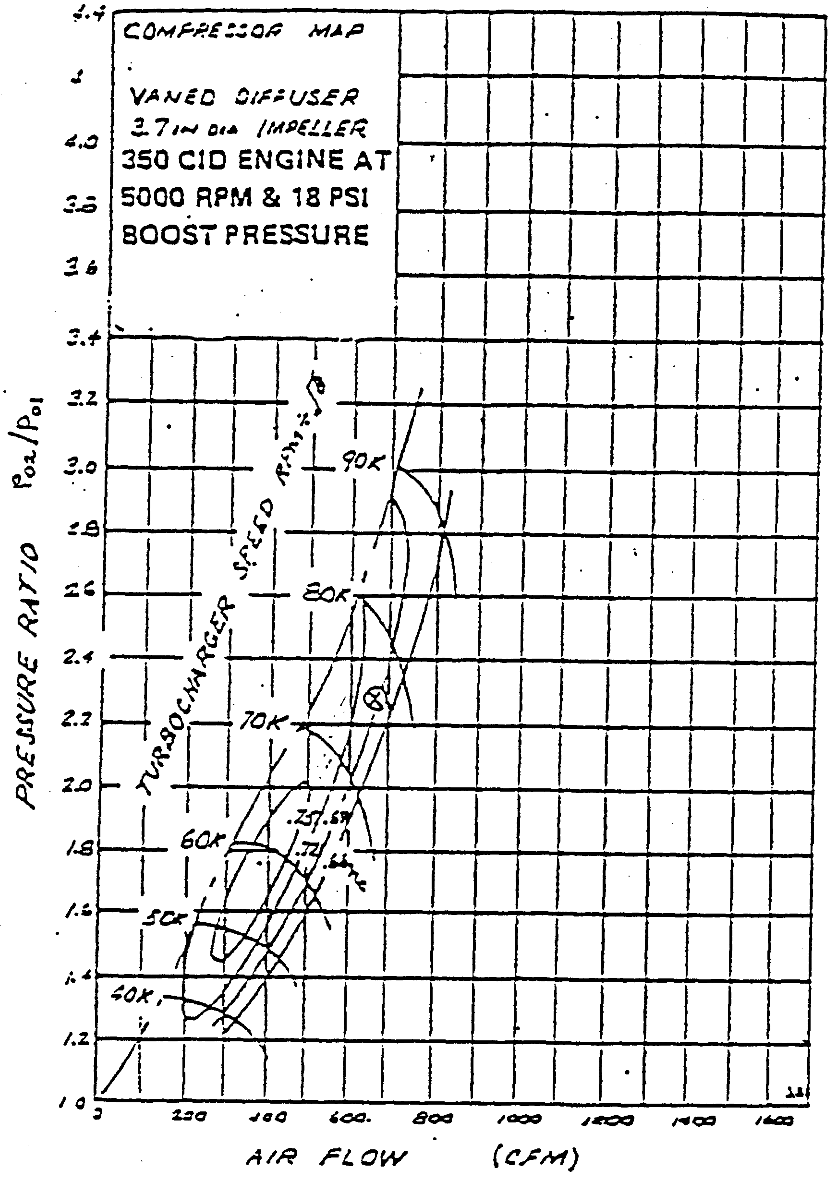

Figure 1-2: Typical centrifugal compressor map. Vaned

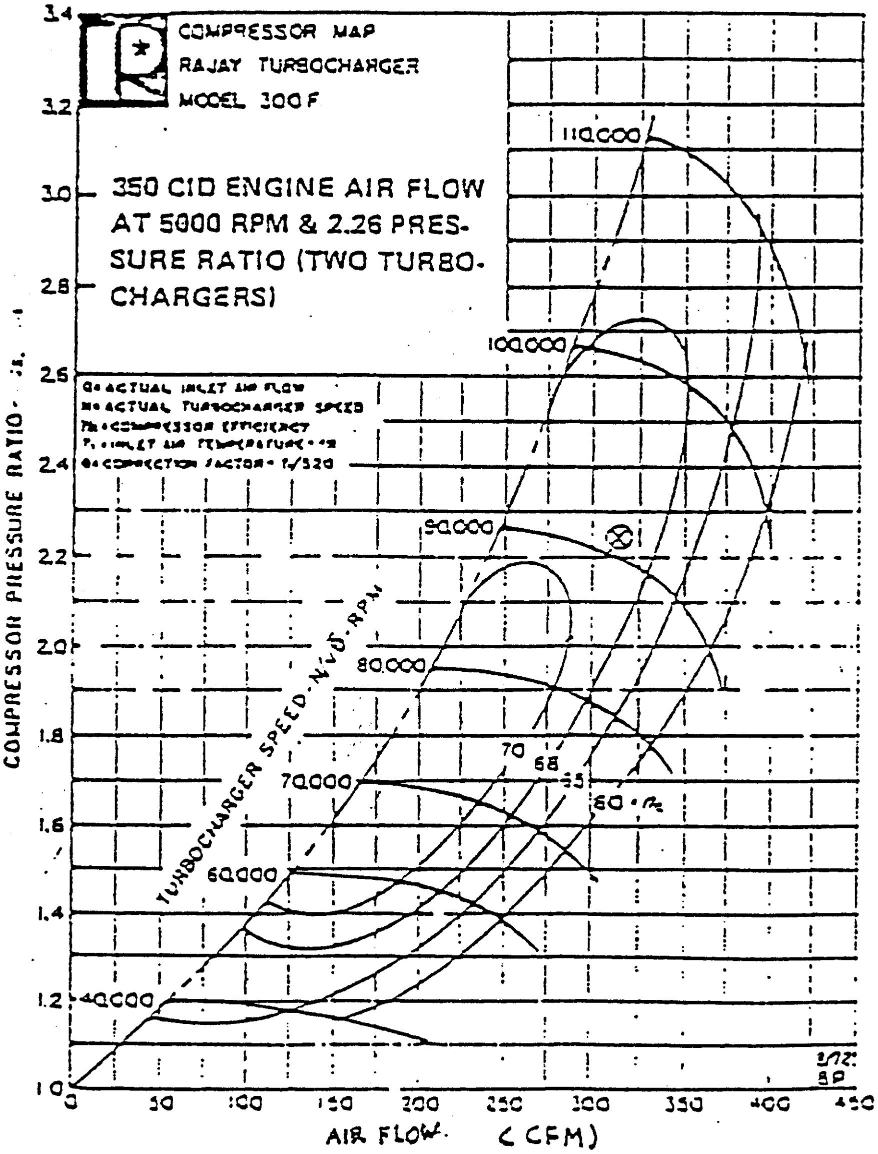

Figure 1-3: Typical centrifugal compressor map Vaneless

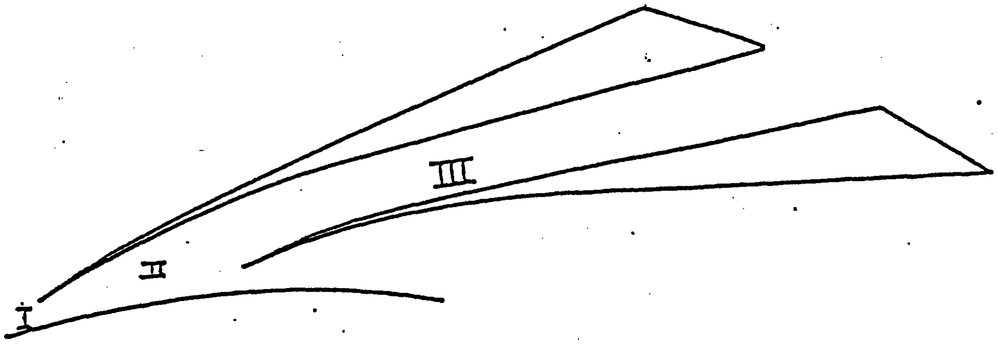

Figure 1-4: Flow regions of the vaned diffuser

The present investigation serves as a preliminary assessment of the merit of Campbell diffuser design concept applied to supersonic flow. In order to save time and effort, only the performance of the Campbell diffuser at design point is studied and compared with that of parallel end walls diffusers with the same vane shape. A more thorough calculation over different impeller speed and mass flow rate can be followed if the Campbell diffuser design is found to outperform the parallel end walls diffusers.

1.5 Method of investigation

A numerical simulation is used to investigate the flow fields of the different diffuser configurations. The calculation involves solving inviscid three-dimensional Euler equations.

The flow field in the impeller exit/diffuser entry region is complex and the fluid dynamics in that region is not well understood. The flow is highly turbulent and unsteady. It is unsteady in the absolute (diffuser) and relative (impeller) coordinates. The unsteadiness in the absolute frame is due to the non-uniformity of the flow leaving the impeller and the unsteadiness in the relative frame is due to the presence of the diffuser vanes. The unsteady pressure fluctuations at the diffuser throat is of the order of 10% of the mean value. Boundary layers grow rapidly on the side walls under the influence of the adverse pressure gradient at the diffuser entry. These boundary layers are turbulent and three-dimensional. The situation is further complicated by the interaction between the impeller blade tip and the diffuser vanes. The Mach number in the diffuser entry is about 1.1 and shocks will occur in the flow. Shock wave-boundary layer interaction should be taken into consideration [2, 12]. Certain assumptions are made to simplify the situation. The inlet flow is assumed to be steady and uniform, i.e. there is no interaction between the impeller and the diffuser. The flow is assumed to be steady, inviscid and adiabatic. As the first step of the investigation, the boundary layer blockage is ignored. The author is aware that without taking into consideration of blockage, one cannot hope to obtain a realistic solution. However, analysis of the inviscid flow field will be helpful for defining the fluid dynamic behavior of the flow and hence determine the performance of the diffusers.

The advantage of using inviscid Euler equations is that the solution can be obtained with a reasonable amount of computational resource. Unlike experimental study, numerical simulation can separate the influence of diffuser geometry, inlet conditions and unsteadiness easily by using the simpler flow model. It provides a faster and cheaper mean for a parametric study of different diffuser configurations.

Chapter 2

Diffuser Configurations

2.1 Introduction

Four diffusers are used to investigate the effect of Campbell diffuser concept. It is thought that the diffuser configurations chosen in the present investigation are enough to illustrate the Campbell diffuser concept [14]. Two of them are two-dimensional diffusers i.e. vaned diffusers with axisymmetric end walls. The others are constructed by changing the end walls of the two-dimensional diffuser in a non-axisymmetric way. The detail of the diffuser geometry will be described in this chapter.

2.2 Diffuser design

It has been known that vaned diffusers are the most efficient devices to decelerate the transonic or supersonic flow to achieve desired pressure recovery in a diffuser. There is a wide range of vaned diffuser types. The most commonly used are passage diffusers and airfoil diffusers. Japikse [16] made a good comparison between passage and airfoil diffusers. He pointed out that although several references [4] reported the superiority of the airfoil diffuser, they lacked the necessary industrial verification and proof through application experience. Many manufacturers avoid using airfoil diffusers. Instead they use well-known vaneless diffusers, straight wall channel diffusers or pipe diffusers to meet their diffuser needs.

A vane island diffuser is chosen for the investigation. A wide range of curved vane island diffusers were evaluated by Sagi and Johnston [17] under uniform inlet condition. They showed that the straight center diffusers had a better performance than the curve ones (see fig. 2-1)

Two different diffusers vane leading edges are used. One is with straight leading edge on pressure side up to the throat while the other is with parabolic shape pressure side up to the throat. The shape of the vane suction surface is so designed that it nearly coincides with a spiral streamline in an unperturbed free vortex flow. Aft the throat, a divergent channel with straight center-line is used.

The number of vanes employed in vane island diffusers in contemporary practice can vary from 8 to 60 [2]. There is no clear preference of certain number of vanes. A low number of vanes stabilize the shock at entry but reduce the channel diffuser performance. In the present investigation, 31 vanes are used.

2.3 Choice of design parameters

Precise diffuser recovery prediction is still not possible from any existing theory. A careful design of suction side surface shape is required to limit the strength of the shock upstream of the throat. There are relatively few performance data for high speed centrifugal diffusers on the open literature. As we have mentioned in the above, the vane suction side surface nearly coincides with a spiral streamline in an unperturbed free vortex flow.

The operating point is chosen to maximize the diffuser recovery. According to Osborne [15], it can be achieved by setting the Mach number at the throat as high as possible (with a limit of one) consistent with flow range requirements (both to choke and to surge). The impeller exit Mach number is chosen to be about 1.14 with an absolute swirl angle of 71°. The exit pressure is adjusted so that it corresponds to that at the

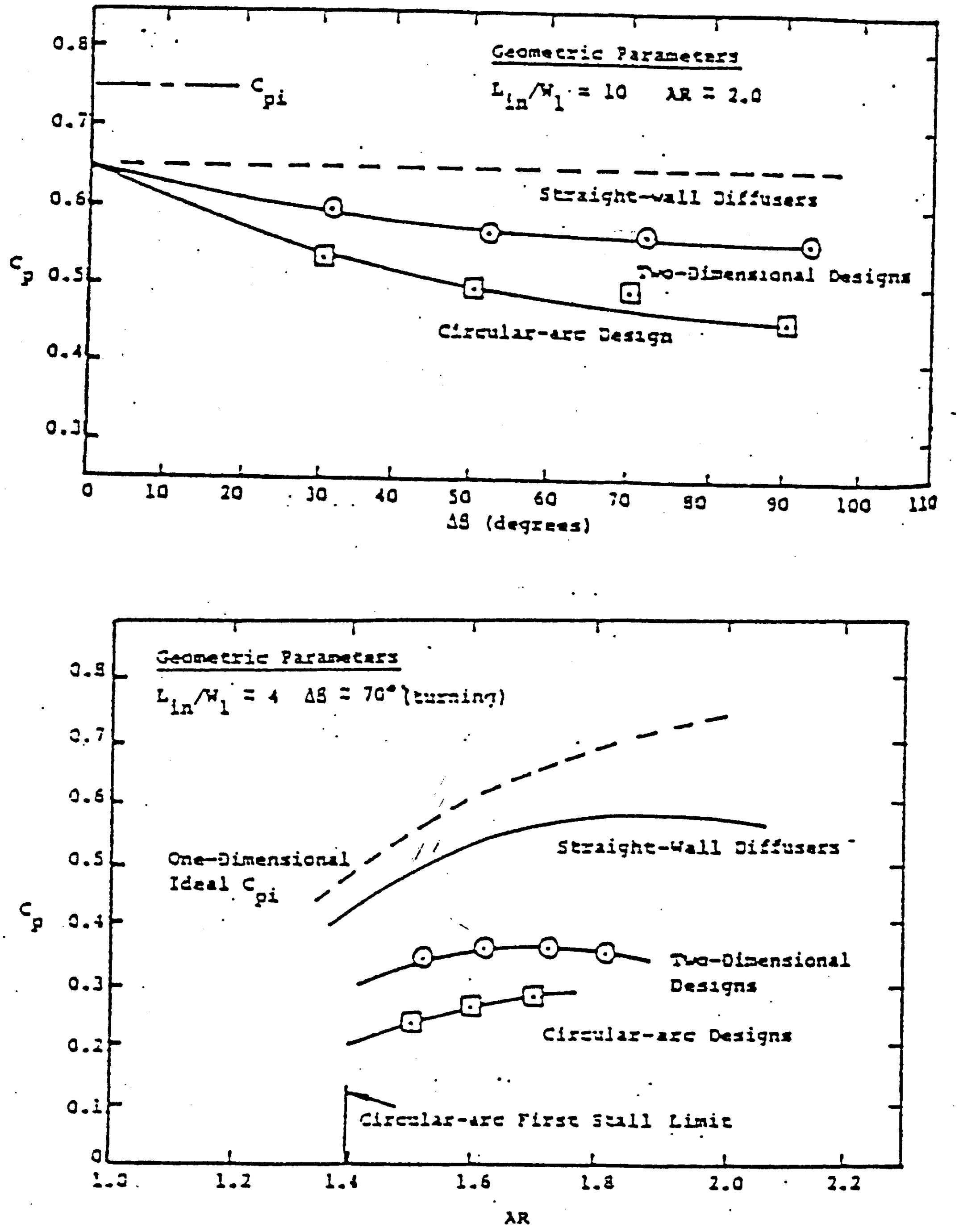

Figure 2-1: Comparison of curved and straight centerline channel diffusers

operating point. The exit pressure is not known in priori; it can only be estimated by 1D analysis and then adjusted to the correct value during the course of the calculation. The calculation of supersonic diffusers is very sensitive to the pressure ratio imposed [18]. A slightly high pressure ratio can reverse the flow direction while too low pressure ratio will move the operation to choke line. When the flow is choked, the shock moves into the subsonic channel through an undesirable reacceleration from the sonic throat.

2.4 Detail of diffuser geometry

Four diffuser configurations are chosen for the present computational investigation:

1. A straight vane leading edge with parallel end walls (i.e. with axisymmetric end walls).
2. A straight vane leading edge with non-axisymmetric end walls.
3. A parabolic vane leading edge with parallel end walls (i.e. with axisymmetric end walls).
4. A parabolic vane leading edge with non-axisymmetric end walls..

The parameters that characterize the diffuser geometry is delineated in Table 2.1; the vane shape for that with a straight leading edge is shown in figure 2-2 while for that with a parabolic leading edge is in figure 2-3. The location of the diffuser throat is also indicated in the figures.

In the non-axisymmetric cases, the diffusers have parallel end walls at its entrance and exit. On the pressure side, the end wall passage depth converges to half the passage width of the inlet (0.3 inch) at the throat and then expands back to the original depth at diffuser exit. The passage profile of the pressure side and that of the suction side

diffuser parameter	description
$r_3/r_2 = 1.025$	radius ratio diffuser leading edge/impeller exit
$r_4/r_2 = 1.32$	radius ratio diffuser discharge/impeller exit
$\delta/r_2 = 0.06$	ratio of passage depth to impeller exit
$2\theta = 7^o$	channel divergence angle
$Z_d = 31$	vane number

Table 2.1: Diffuser parameters

are shown in figure 2-4 and figure 2-5 respectively. For a fair comparison, the area distributions of the two cases should be the same. Therefore, the end wall passage width of the suction side is contoured in such a way that the one dimensional area distribution along the meridional direction is the same as the parallel end walls case. The passage width varies linearly from blade-to-blade across a plane perpendicular to the meridional plane.

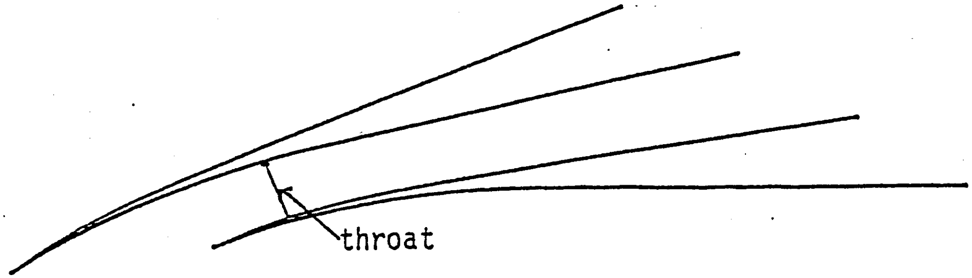

Figure 2-2: Straight leading edge blade

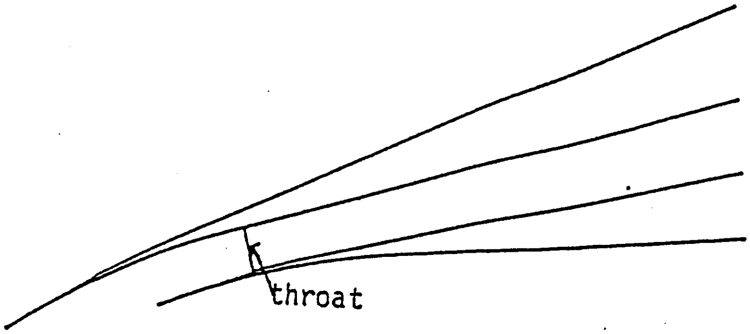

Figure 2-3: Parabolic leading edge blade

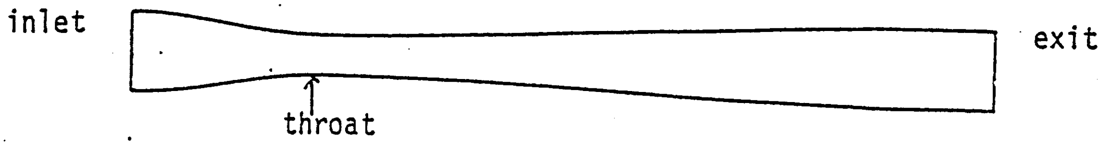

Figure 2-4: Pressure side passage profile

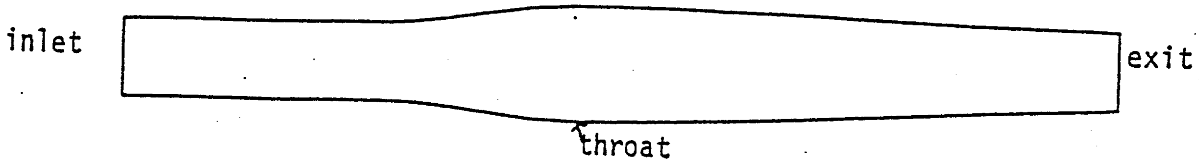

Figure 2-5: Suction side passage profile

Chapter 3

Computational Algorithm

3.1 Introduction

The computational code [19] for the present computational investigation was developed by J. Adamczyk et al at NASA Lewis research center. It is based on the Jameson's finite volume time stepping scheme [20]. Although the code was originally written for axial turbomachinery, modifications have been made to tailor the program for the present study. The modifications are in the inflow and outflow boundary conditions and will be discussed in a later section.

3.2 Governing equations

The Euler equations are written in cylindrical coordinate system. Here, we have used r to denote the radial coordinate, θ the tangential coordinate and z the axial coordinate; the corresponding velocity components are denoted by v_r, v_θ and v_z. In vector form, the Euler equation can be written as

$$\frac{\partial}{\partial t}\int \vec{U} dVol + L(\vec{U}) = \int K dVol \tag{3.1}$$

with

$$\vec{U} = \begin{bmatrix} \rho \\ \rho v_r \\ r\rho v_\theta \\ \rho v_z \\ \rho e_0 \end{bmatrix}$$

$$L(\vec{U}) = \int_{dA} [F \cdot dA_r + G \cdot dA_\theta + H \cdot dA_z]$$

where

$$F = \begin{bmatrix} \rho v_r \\ \rho v_r^2 + P \\ r\rho v_\theta v_r \\ \rho v_z v_r \\ \rho h_0 v_r \end{bmatrix}$$

$$G = \begin{bmatrix} \rho v_\theta \\ \rho v_r v_\theta \\ r(\rho v_\theta^2 + P) \\ \rho v_z v_\theta \\ \rho h_0 v_\theta \end{bmatrix}$$

$$H = \begin{bmatrix} \rho v_z \\ \rho v_r v_z \\ r\rho v_\theta v_z \\ \rho v_z^2 + P \\ \rho h_0 v_z \end{bmatrix}$$

$$K = \begin{bmatrix} 0 \\ (\rho v_\theta^2 + P)/r \\ 0 \\ 0 \\ 0 \end{bmatrix}$$

The vector $\vec{U}$ consists of the following flow variables: density (ρ), axial and radial momenta (ρv_z and ρv_r), angular momentum ($\rho r v_\theta$) and total internal energy (ρe_0). The operator L($\vec{U}$) is a flux operator for the mass, axial and radial momenta, angular momentum and energy through an elemental control volume $dVol$, whereas $\int KdVol$ can be viewed as a source term due to the use of cylindrical coordinate system.

Upon using the equation of state, the total internal energy can be related to the pressure P as follows

$$e_0 = \frac{P}{\rho(\gamma - 1)} + \frac{1}{2}(v_r^2 + v_\theta^2 + v_z^2)$$

;the total enthalpy h_0 can be related to e_0 and P by

$$h_0 = e_0 + \frac{P}{\rho}$$

We are interested in using the inviscid steady state solution for evaluating the performance of the diffusers. Thus in the solution procedure, the unsteady Euler equation is allowed to evolve in time until it achieves an asymptotic steady state. This can be done with the choice of Jameson's scheme for the discretization of the unsteady Euler equation written in the form of eqn.(3.1).

3.3 Nondimensionalization and discretization

Before we begin to apply discretization to eqn.(3.1), it is useful to make all variables nondimensional with respect to characteristic quantities in the situation of interest here. We have found it appropriate to nondimensionalize all lengths by the diffuser inlet radius; the

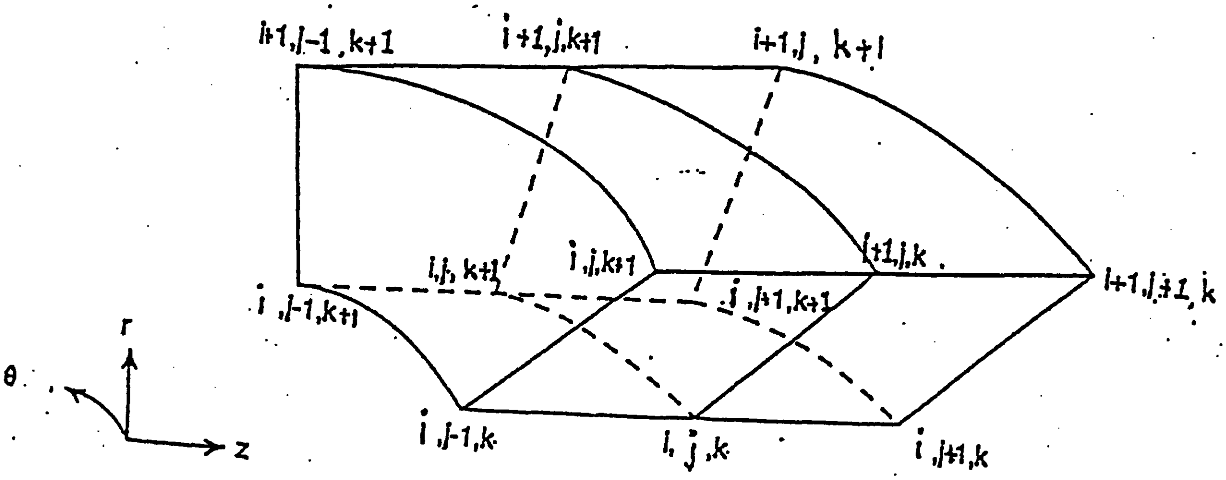

Figure 3-1: A typical computational cell

velocity, pressure, and density by the far upstream stagnation pressure and density. To be more specific, in non-dimensional term we would have (with ^ indicating dimensional quantity),

$$r = \frac{\hat{r}}{\hat{r}_{ref}}; v = \frac{\hat{v}}{\sqrt{\hat{P}_{0ref}/\hat{\rho}_{0ref}}}; P = \frac{\hat{P}}{\hat{P}_{0ref}}$$

$$z = \frac{\hat{z}}{\hat{r}_{ref}}; \rho = \frac{\hat{\rho}}{\hat{\rho}_{0ref}}; \dot{m} = \frac{\hat{\dot{m}} c_1}{\hat{P}_{0ref}\hat{r}^2}$$

where

$$c_1 = \sqrt{\frac{\hat{P}_{0ref}}{\hat{\rho}_{0ref}}}$$

$\hat{r}_{ref}$ is the diffuser inlet radius, $\hat{P}_{0ref}$ the stagnation pressure at inlet and $\hat{\rho}_{0ref}$ the stagnation density at inlet. Note that c_1 may be viewed as a stagnation sound speed (in fact it is γc_1). With the above nondimensionalization scheme, we can now proceed to discretize eqn.(3.1) in space and time.

Equation 3.1 is discretized in space for a cell volume as shown in Figure 3-1 by approximating the surface integrals with the midpoint rule. The resulting semi-discrete equations form a system of ordinary differential equations of the form

$$\frac{d}{dt}(\vec{U}) + \frac{1}{V}\sum[FdA_r + GdA_\theta + HdA_z] = K \tag{3.2}$$

where V is the volume of a cell.

The surface areas, dA_r,dA_θ,dA_z are calculated using the cross product of the diagonals of a cell face and the volume is determined using the formula described by Holmes and Tong [21]. All the flow variables are cell-centered. The value of a variable at any surface, except at solid boundaries, is determined by taking the average of that variable for the two neighboring cells. The above discretization scheme simply reduces to that of second order accurate central differencing for a uniform mesh [20].

3.4 Time integration

A four-stage Runge-Kutta scheme [20] is adopted to advance equation(3.2) in time. It can be written as

$$\begin{aligned}
\vec{U}_1 &= \vec{U}^n - \alpha_1\Delta t(\frac{L(\vec{U}^n)}{V} + K^n) \\
\vec{U}_2 &= \vec{U}^n - \alpha_2\Delta t(\frac{L(\vec{U}^1)}{V} + K^1) \\
\vec{U}_3 &= \vec{U}^n - \alpha_3\Delta t(\frac{L(\vec{U}^2)}{V} + K^2) \\
\vec{U}_4 &= \vec{U}^n - \alpha_4\Delta t(\frac{L(\vec{U}^3)}{V} + K^2) \\
\vec{U}^{n+1} &= \vec{U}_4 + \frac{1}{V}D(\vec{U}_4)
\end{aligned} \tag{3.3}$$

where

$$\alpha_1 = 1/4$$

$$\alpha_2 = 1/3$$

$$\alpha_3 = 1/2$$

$$\alpha_4 = 1$$

and $D(\vec{U})$ is the dissipation operator.

The maximum permissible time step for this is restricted by CFL stability limit. The CFL stability limit was found by Jameson [20] to be $2\sqrt{2}$. Since we are only interested in obtaining steady state solution, a local time step is chosen to maximize the CFL number and hence accelerates the converging rate.

3.5 Artificial dissipation

To suppress the odd-even point decoupling and to prevent the appearance of wiggles in regions containing severe pressure gradients in the neighboring of shocks waves or stagnation points, Jameson [20] developed a blend of second and fourth order difference smoothing operators through extensive numerical experiments. The fourth order artificial viscosity has the following form

$$D_{ijk}^{(4)} = -\left\{\delta_{x_i}\left(\frac{V_{ijk}}{\Delta t_{ijk}}\epsilon_{ijk}^{(4)}\delta_{x_i}^3\vec{U}_{ijk}\right) + \delta_{x_j}\left(\frac{V_{ijk}}{\Delta t_{ijk}}\epsilon_{ijk}^{(4)}\delta_{x_j}^3\vec{U}_{ijk}\right) + \delta_{x_k}\left(\frac{V_{ijk}}{\Delta t_{ijk}}\epsilon_{ijk}^{(4)}\delta_{x_k}^3\vec{U}_{ijk}\right)\right\} \quad (3.4)$$

where

V_{ijk} is the cell volume

δ_{x_i} is the central difference operator

Δt_{ijk} is the time step for a cell, scaled to a CFL number of 1

$\epsilon_{ijk}^{(4)} = \max(0, 1/32 - \nu_{ijk})$

The fourth difference dissipation provides a background dissipation to stabilize the time stepping scheme. However, it will have a destabilizing effect near the shock where the pressure gradient is high. It will be turned off near the shock and a second difference is used to capture the shock. The second difference artificial viscosity is of the form

$$D^{(2)}_{ijk} = \left\{ \delta_{x_i}\left(\frac{V_{ijk}}{\Delta t_{ijk}}\epsilon^{(2)}_{ijk}\delta_{x_i}\vec{U}_{ijk}\right) + \delta_{x_j}\left(\frac{V_{ijk}}{\Delta t_{ijk}}\epsilon^{(2)}_{ijk}\delta_{x_j}\vec{U}_{ijk}\right) + \delta_{x_k}\left(\frac{V_{ijk}}{\Delta t_{ijk}}\epsilon^{(2)}_{ijk}\delta_{x_k}\vec{U}_{ijk}\right) \right\} \tag{3.5}$$

where

$$\begin{aligned} \epsilon^{(2)}_{i+\frac{1}{2}\,jk} &= \min(0.25, 2\nu_{ijk}) \\ \nu_{ijk} &= \left| \frac{P_{i+1,j,k} - 2P_{i,j,k} + P_{i-1,j,k}}{P_{i+1,j,k} + 2P_{i,j,k} + P_{i-1,j,k}} \right| \end{aligned}$$

The variable v_{ijk} is proportional to the square of the mesh spacing in smooth pressure field region and linear in mesh spacing in regions of large pressure gradients. This pressure sensitive switch makes it possible to capture shock sharply and retain second order accuracy away from shocks. Thus $D(\vec{U})$ operator combines the second and fourth difference terms to give

$$D_{ijk} = D^{(2)}_{ijk} + D^{(4)}_{ijk}$$

3.6 Boundary conditions

Boundary conditions on the computational domain are required to solve the system of equations. However, we may not be able to get sufficient boundary conditions to close the system. Extra relations are derived from local analysis.

Periodic boundary condition is imposed upstream of the blades. The flow will exhibit a spatial periodicity equal to the pitch of the blade row. Any information required from cells outside the computational domain can be obtained from their corresponding cells inside the computational domain. One of the advantages of using periodic boundary is that it can give the unique incidence of the flow which is not known beforehand.

At solid surfaces, the requirement of no flux through the walls is applied. For the continuity and energy equations, this can be implemented by setting

$$\vec{u} \cdot \hat{n} = 0 \tag{3.6}$$

where $\hat{n}$ is the unit normal at the surface, $\vec{u}$ is the velocity vector. However in the momentum equation, there is a pressure contribution at the solid wall. The pressure is extrapolated from the interior using the normal momentum equation formulated by Rizzi [22]. The expression is obtained by writing the momentum equation at the wall and dotting it with the unit normal [23],

$$\frac{\partial \vec{u}}{\partial t} \cdot \hat{n} + (\vec{u} \cdot \nabla)\vec{u} \cdot \hat{n} = -\frac{1}{\rho}\nabla p \cdot \hat{n} \tag{3.7}$$

Using eqn.(3.6) and noting that $\partial \hat{n}/\partial t = 0$ for stationary solid boundary, the momentum equation may be rewritten as

$$\vec{u} \cdot (\vec{u} \cdot \nabla \hat{n}) = \frac{\partial p}{\partial n} \tag{3.8}$$

Equation (3.8) gives the pressure gradient normal to the solid surface in term of the surface curvature and the velocity at the wall. The velocity at the wall is taken to be the tangential component of the velocity in the first computational cell off the body; $\partial p/\partial n$ at the wall is computed using eqn.(3.8), and the pressure is extrapolated to the wall from the first interior cell. Solid boundary condition is imposed from leading edge to the end of computational domain. This is due to a complexity in grid generation at trailing edge as we shall see subsequently in the next chapter.

The flow at the inlet has a subsonic radial component, so only four quantities are specified. They are the axial velocity v_z which is zero, the circulation rv_θ, stagnation pressure P_0 and stagnation density ρ_0. In the absence of external torque (which is true in the case of diffusers), the circulation cannot change. So physically it is correct to specify the circulation at the inflow. Denton [24] has pointed out that this condition must be used when the inflow Mach number is supersonic. He found that by specifying the circulation, the calculation will then automatically satisfy the unique incidence condition.

We need one more quantity to close the system and this is given by the Riemann invariant. Riemann invariant J_- based on the radial velocity is extrapolated from the interior domain. The radial velocity v_r is obtained by solving the following equations

$$J_- = v_r - 2\frac{a}{\gamma - 1} \tag{3.9}$$

$$T_0 = T(1 + \frac{\gamma - 1}{2} M^2) \tag{3.10}$$

At the exit, the flow is subsonic. We specified the static pressure and extrapolate the axial velocity, the entropy, the Riemann invariant J_+ and the circulation rv_θ. The Riemann invariant J_+ is associated with the information originating from the computational domain. We extrapolate the circulation because there is no external torque. The density is calculated from

$$\frac{P}{\rho^\gamma} = \exp(s) \tag{3.11}$$

and then radial velocity v_r is obtained from

$$J_+ = v_r + 2\frac{a}{\gamma - 1} \tag{3.12}$$

3.7 Convergence

The convergence history for the four cases are shown in fig. 3-2 to 3-5. The convergence parameters chosen are the time derivative of density $(d\rho/dt)$ and L_2 norm of the change of the flow variables over the entire computational domain. L_2 is defined as

$$L_2 = \sqrt{\sum_{l=1}^{5} \sum_{ijk} (U^n_{l,ijk} - U^{n-1}_{l,ijk})^2}$$

where $U_{l,ijk}$ is the lth component of the state vector $\vec{U}$ at the ijkth cell. The average value of $(d\rho/dt)$ is determined by evaluating the sum of the absolute value of the time derivative at each point in the field divided by the number of points. The jumps in the curves are due to adjustments made in the exit pressure to optimize the operating condition because one does not know the exit pressure at optimal operating condition a priori. Typical convergence history are shown in fig. 3-6 to 3-9; they show the L_2 norm of the difference of the averaged solutions calculated between two time steps. The computations are assumed to have converged when there is a drop of two orders of magnitude in both $(d\rho/dt)$ and the L_2 norm.

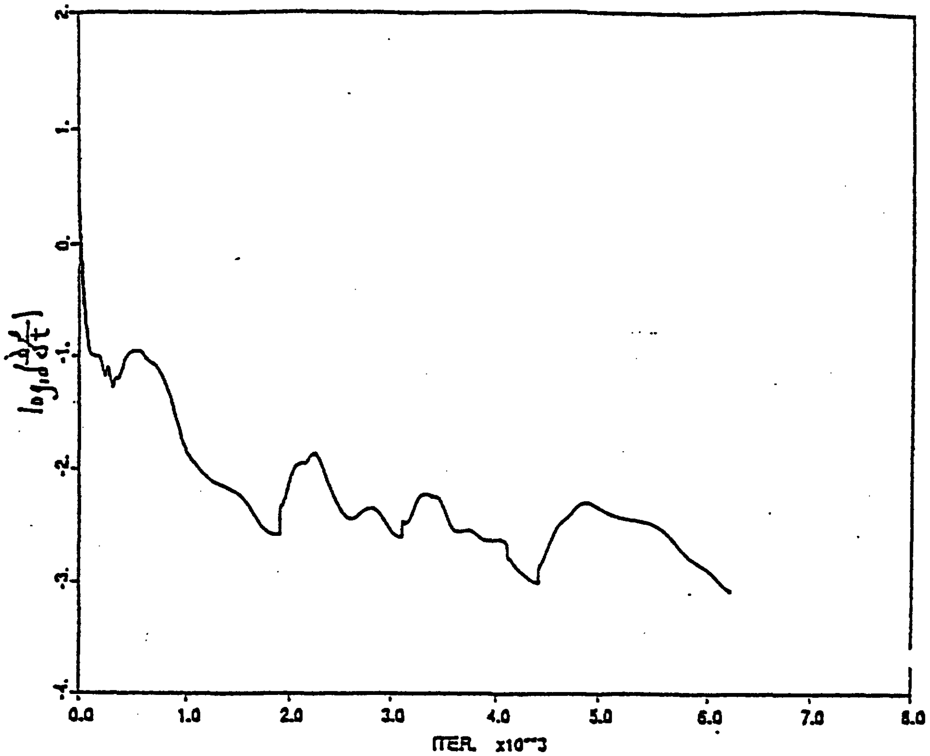

Figure 3-2: Convergence history of the diffuser with straight leading edge and parallel end walls

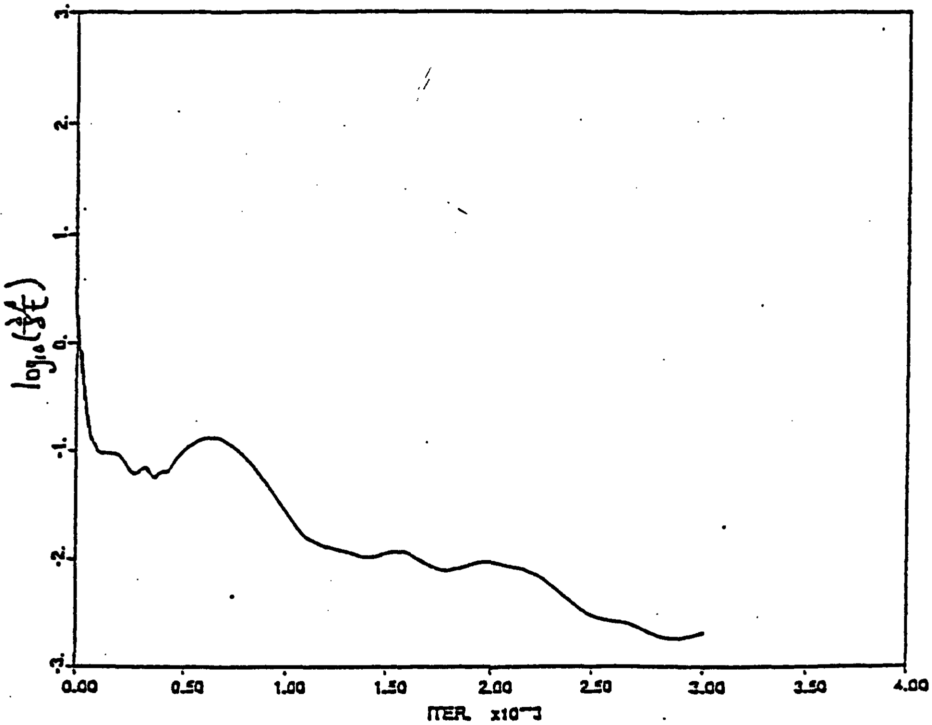

Figure 3-3: Convergence history of the diffuser with straight leading edge and non-axisymmetric end walls

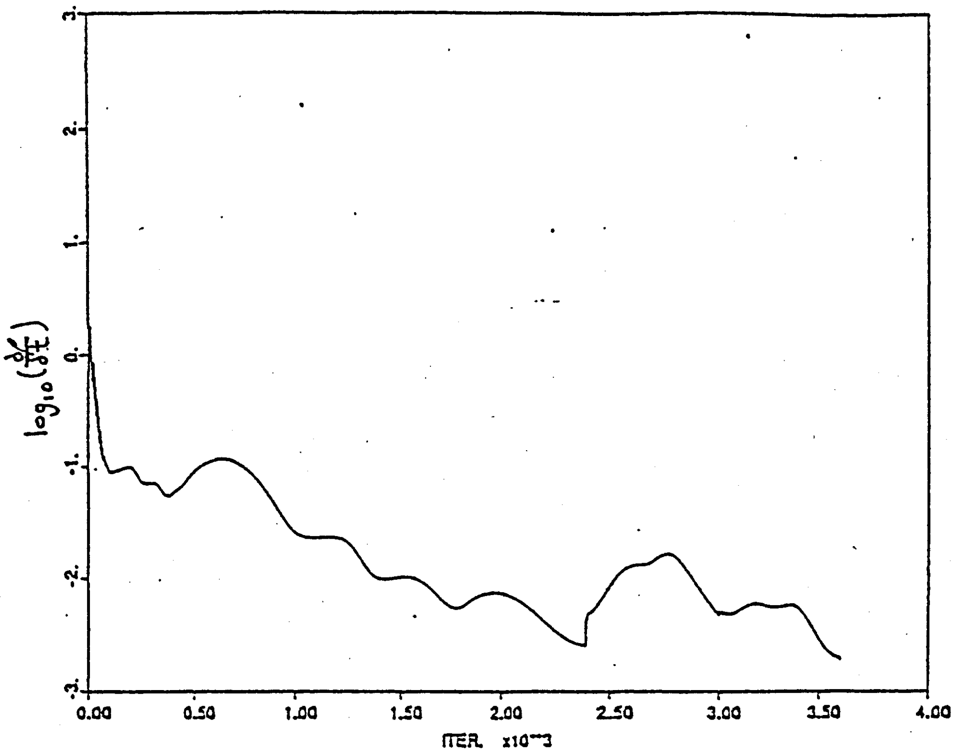

Figure 3-4: Convergence history of the diffuser with parabolic leading edge and parallel end walls

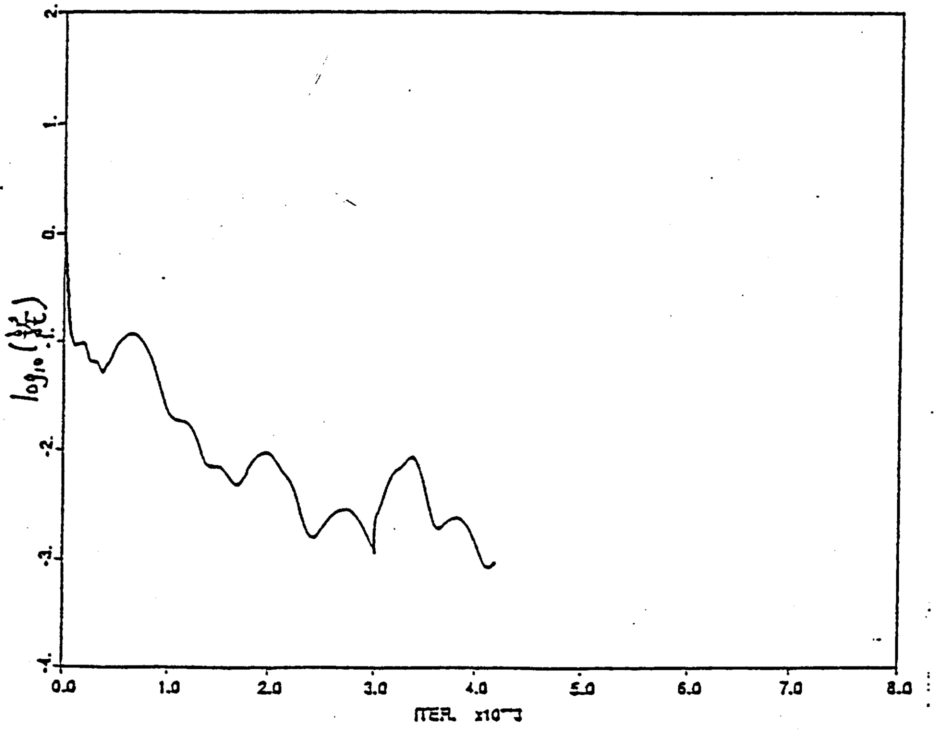

Figure 3-5: Convergence history of the diffuser with parabolic leading edge and non-axisymmetric end walls

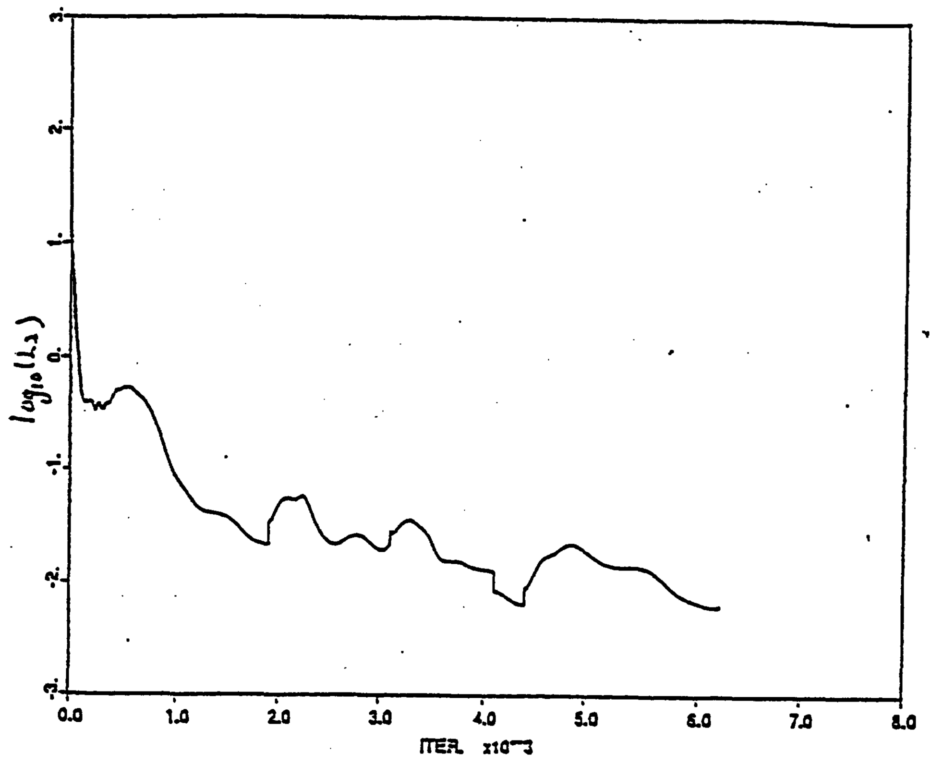

Figure 3-6: L_2 norm of the diffuser with straight leading edge and parallel end walls

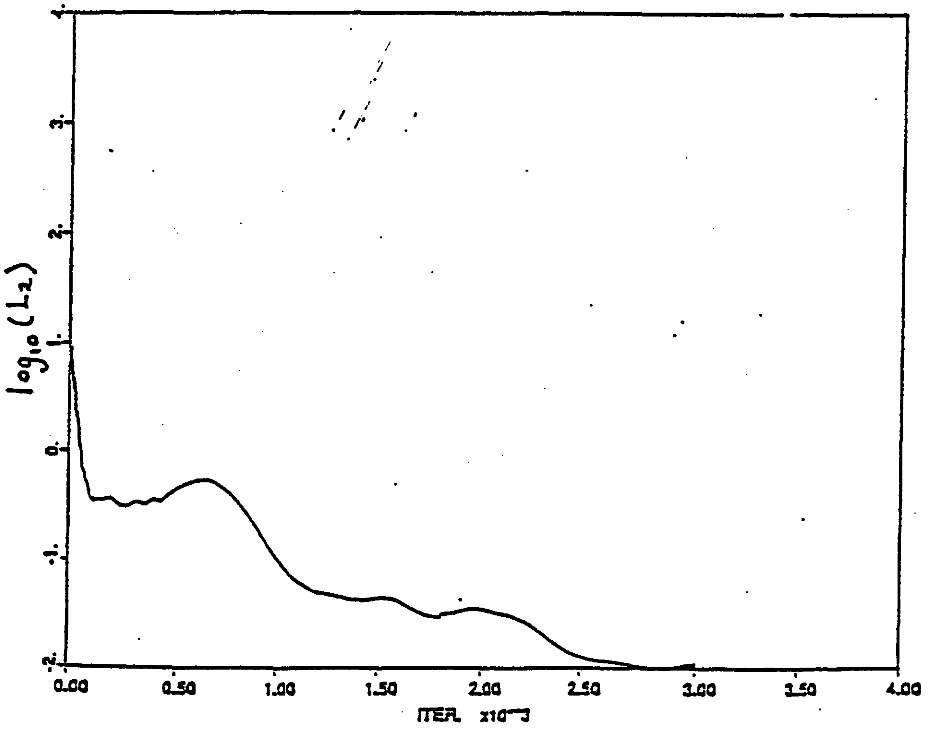

Figure 3-7: L_2 norm of the diffuser with straight leading edge and non-axisymmetric end walls

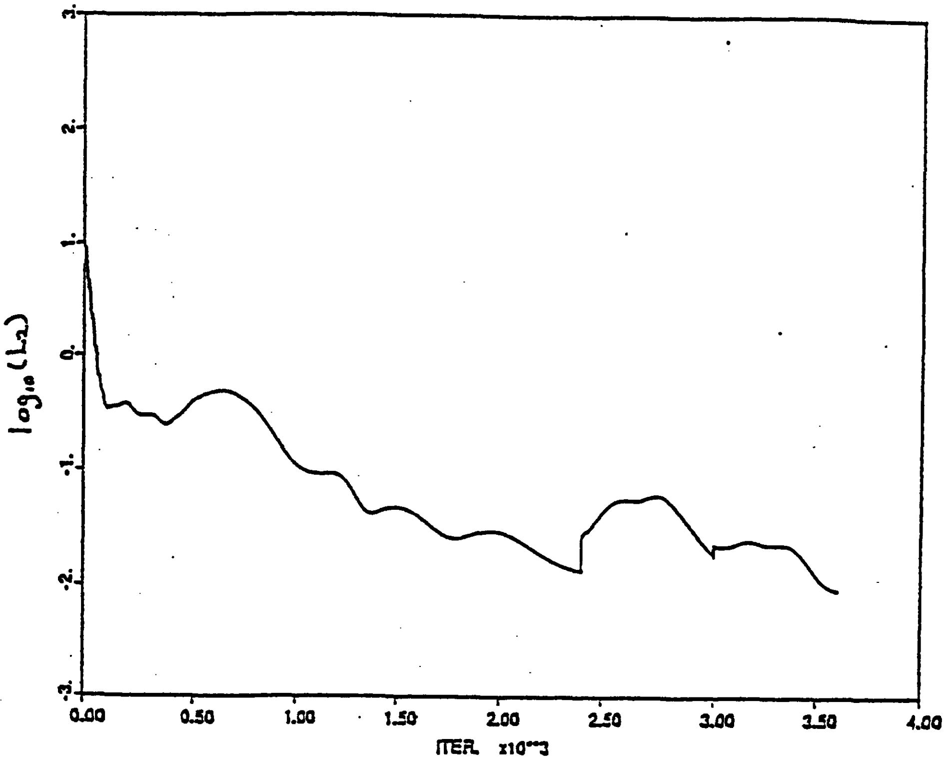

Figure 3-8: L_2 norm of the diffuser with parabolic leading edge and parallel end walls

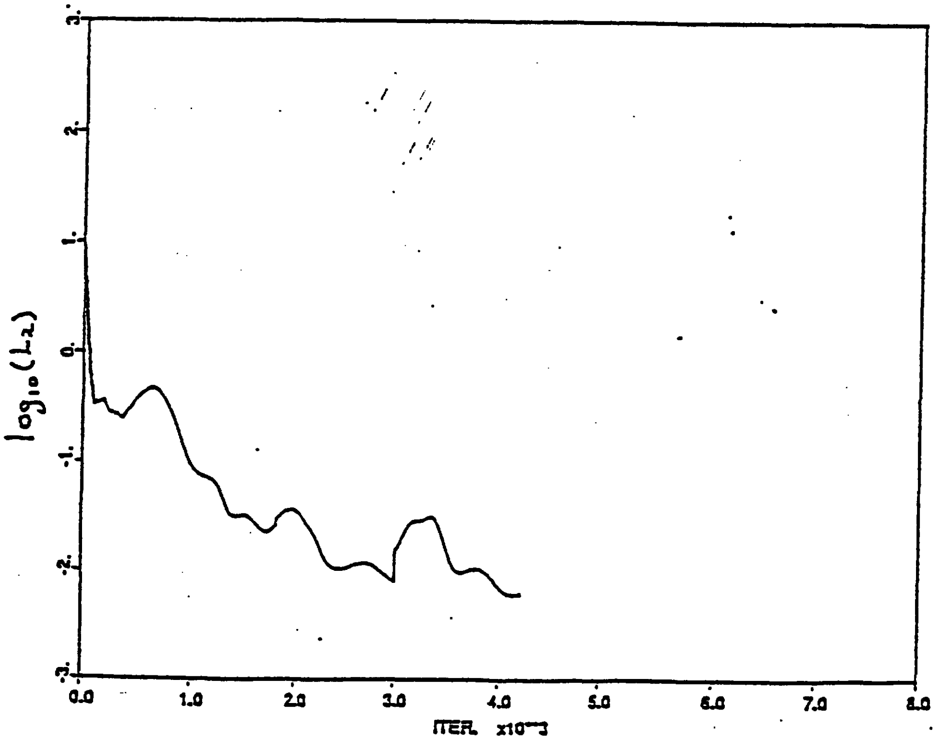

Figure 3-9: L_2 norm of the diffuser with parabolic leading edge and non-axisymmetric end walls

Chapter 4

Grid Generation

4.1 Introduction

A smooth grid is essential for accurate computation. Since entropy is to be used as a measure of the goodness of computation results as well as the performance of diffusers, spurious entropy generation due to an inappropriate grid (such as a non smooth grid, a highly skewed grid) should be minimized as far as possible. In the inviscid flow model, entropy is generated by shock waves only. The artificial smoothing operators in the computational scheme can generate entropy numerically. We attempted to separate the physically valid entropy generation from the numerical one through a careful examination of the computed pressure field. The entropy generation can be viewed to be of physical origin if it is associated with the shock.

Calculation for all the four diffuser configurations were done with the use of H-type grids. The blade-to-blade grids (on the $r - \theta$ plane) have been generated through the numerical solution of a system of elliptic equations [25]. This technique of grid generation will be described in more detail in section 4.2. A typical H-type grid is shown in figure 4-1.

As the diffuser configuration is three dimensional, the three-dimensional grid has been generated by stacking several blade-to-blade grids from one end wall to the other

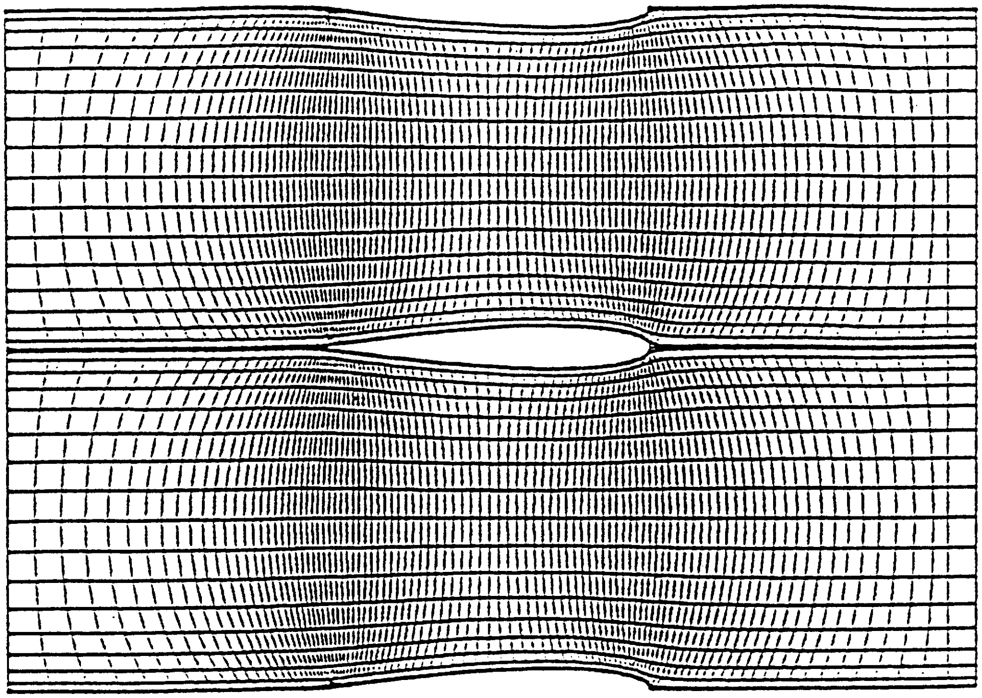

Figure 4-1: A typical H-type grid

end wall. For the diffuser with parallel end walls, the procedure is direct. However for the diffuser with non-axisymmetric end walls, we start with the corresponding two-dimensional diffuser grid, and then rescale the hub to shroud distance according to the conditions specified in chapter 2 to form a 3D grid.

4.2 Mathematical development of 2D grid generation

A brief description of the generation of boundary-fitted curvilinear coordinate systems is presented here. Complete detail can be found in Ref. [26, 27].

The curvilinear coordinates are generated by solving an elliptic system of the form

$$\begin{aligned} \xi_{xx}+\xi_{yy}&=P(\xi,\eta) \\ \eta_{xx}+\eta_{yy}&=Q(\xi,\eta) \end{aligned} \tag{4.1}$$

with Dirichlet boundary conditions, one coordinate being specified to be equal to a constant on the pressure side and the other equal to another constant on the suction side.

$P(\xi,\eta), Q(\xi,\eta)$ are the functions that control the spacing of the grid lines. As suggested by Thompson [26, 27] P and Q can be chosen to be the followings:

$$\begin{aligned} P(\xi,\eta) \equiv\ & -\textstyle\sum_{i=1}^{n} a_i sgn(\xi - \xi_i) exp(-c_i|\xi - \xi_i|) \\ & -\textstyle\sum_{j=1}^{m} b_j sgn(\xi - \xi_j) exp(-dj\sqrt{(\xi - \xi_j)^2 + (\eta - \eta_j)^2}) \end{aligned} \tag{4.2}$$

$$\begin{aligned} Q(\xi,\eta) \equiv\ & -\textstyle\sum_{i=1}^{n} a_i sgn(\eta - \eta_i) exp(-c_i|\eta - \eta_i|) \\ & -\textstyle\sum_{j=1}^{m} b_j sgn(\eta - \eta_j) exp(-dj\sqrt{(\xi - \xi_j)^2 + (\eta - \eta_j)^2}) \end{aligned} \tag{4.3}$$

where the positive amplitudes a's, b's and decay factors c's, d's can be chosen differently for each equation. The first term of $P(\xi,\eta)$ has an attracting effect on ξ lines to ξ_i's while the second term has an attracting effect on ξ lines to the point (ξ_j,η_j). $Q(\xi,\eta)$ terms attract η lines in the same way.

Eqn.(4.1) is in terms of dependent variables in (ξ,η) domain. However, we want to perform all the numerical computation in the uniform rectangular transformed plane. After interchanging the dependent and independent variables, the equations become

$$\begin{aligned} \alpha x_{\xi\xi} - 2\beta x_{\xi\eta} + \gamma x_{\eta\eta} + J^2(P x_\xi + Q x_\eta) = 0 \\ \alpha y_{\xi\xi} - 2\beta y_{\xi\eta} + \gamma y_{\eta\eta} + J^2(P y_\xi + Q y_\eta) = 0 \end{aligned} \tag{4.4}$$

where

$$\alpha = x_\eta^2 + y_\eta^2$$

$$\beta = x_\xi x_\eta + y_\xi y_\eta$$

$$\gamma = x_\eta^2 + y_\xi^2$$

$$J = x_\xi y_\eta - x_\eta y_{xi}$$

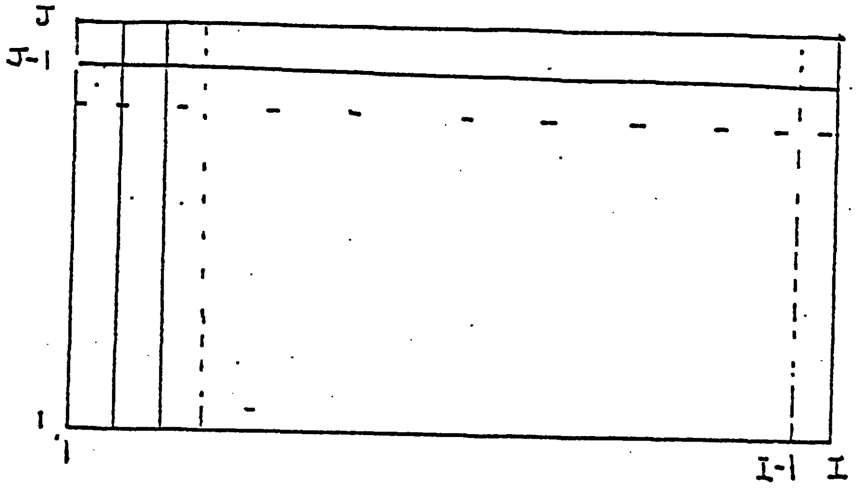

Figure 4-2: Computational domain

4.3 Numerical implementation

As we are solving the inviscid Euler equation, it is not necessary to cluster too many grid lines near the solid surfaces. Only a few terms are added to $Q(\xi,\eta)$ to draw the η lines closer to the solid surfaces to resolve the flow feature at the leading edge region.

All the derivatives in eqn.(4.4) are approximated by second-order central differencing. By choosing $\Delta\xi$ and $\Delta\eta$ to be unity, we arrive at the following expressions

$$\begin{aligned}
(f_\xi)_{ij} &\approx 1/2(f_{i+1,j} - f_{i-1,j}) \\
(f_\eta)_{ij} &\approx 1/2(f_{i,j+1} - f_{i,j-1}) \\
(f_{\xi\xi})_{ij} &\approx f_{i+1,j} - 2f_{ij} + f_{i-1,j} \\
(f_{\eta\eta})_{ij} &\approx f_{i,j+1} - 2f_{ij} + f_{i,j-1} \\
(f_{\xi\eta})_{ij} &\approx 1/4(f_{i+1,j+1} - f_{i+1,j-1} - f_{i-1,j+1} + f_{i-1,j-1})
\end{aligned}$$

The computational domain is as shown in figure 4-2. By specifying the values of (x,y) at inlet, exit and solid boundary, we get a set of 2(I-1)(J-1) nonlinear difference equations,

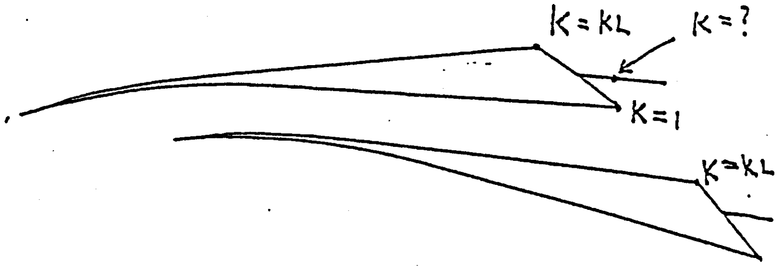

Figure 4-3: Illustration of the problem of closing trailing edge

two for each point(i, j). They are solved by successive over relaxation. The iteration is stopped when the maximum change of the variables (x,y) between iterations is less than 10^{-5}.

4.4 Trailing edge problem

Island vane diffusers have blunt trailing edges which introduce a difficulty in closing the blade to form a periodic boundary downstream of the trailing edge. This point is illustrated in figure 4-3. To overcome this, we have chosen to extend the straight channel to about 10 times the passage width and assume that the flow has achieved a state with uniform static pressure there . As we are interested in examining the influence of contouring end wall in the neighborhood of the throat region, it is quite appropriate to argue that the exit may not-necessarily contaminate the flow field in the region of interest if we choose the exit boundary to be far away from the throat, e.g. 10 throat widths downstream of the diffuser throat location.

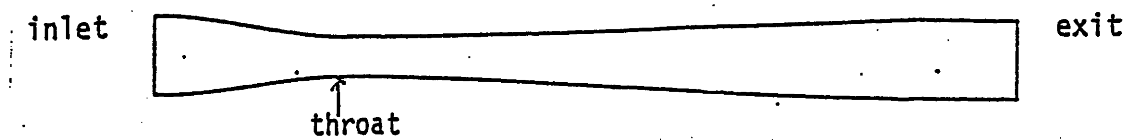

Figure 4-4: The profile of the pressure side of the blade

4.5 Non-axisymmetric diffuser grid generation

The vane pressure side profile is determined and is shown in fig. 4-4. It is symmetric about the center line and consists of two cubic curves both of which have a minimum at the throat. Starting with the corresponding two-dimensional diffuser, the pressure side is rescaled according to the specified profile from leading edge to trailing edge. Then a perpendicular line is drawn from the pressure side leading edge and another perpendicular line is drawn from suction side trailing edge to define the region for rescaling. This is shown in fig. 4-5. Both lines are on the same $r - \theta$ plane. The next step involves the determination of points nearest to the first and second perpendicular lines for every grid line of constant K index. These points are the starting and ending points for rescaling of each grid line. The distances between the starting point and other points on the same grid line have been normalized by the distance between the starting point and the ending point. We call this normalized distance s. Now every point has a value of s ranging from 0 to 1. Rescaling the blade height of the suction side so that the average of the suction

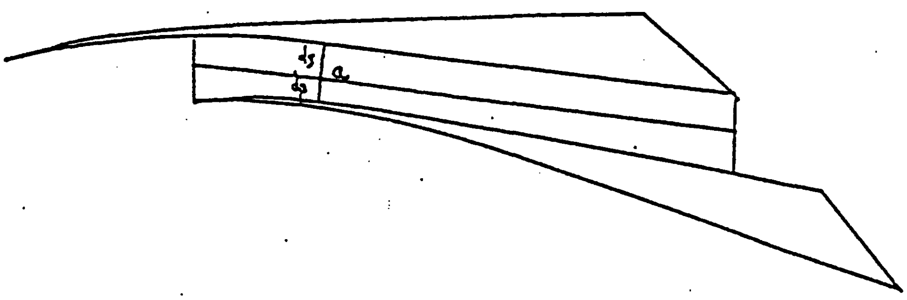

Figure 4-5: The region for rescaling of the two dimensional diffuser on $r - \theta$ plane

side blade height h_s and the corresponding pressure side blade height h_p is the same as that of the parallel end wall case. For example, if a grid point on the suction side has the value of s equals 0.3, then we have to know the blade height of the pressure side at a point where it has the same value of s. In this procedure, the use of interpolation may be necessary. With the knowledge of these corresponding blade heights, we can then compute h_s from $h_s = 2h_o - h_p$, where h_o is the original blade height of the two dimensional diffuser. After defining the profiles of the pressure and suction sides, the hub to shroud distance for interior grid points can be calculated by taking the weighted average of the corresponding pressure and suction side blade heights. The weight function is related to the distances between the grid points and two blades. A typical grid point a in fig 4-5 has the hub to shroud distance given by

$$h_a = \frac{d_s h_p + d_p h_s}{d_p + d_s} \tag{4.5}$$

Total no. of grid points	$106 \times 19 \times 19$
No. of grid points from blade to blade	19
No. of grid points from hub to shroud	19
No. of grid points from inlet to leading edge	37

Table 4.1: Grid information

where d_p is the distance between the grid point and the pressure side of the blade and d_s is the distance between the grid point and the suction side of the blade. Thus, a relatively smooth but complicated surface can be generated by simple scaling.

4.6 Final grids

The information about the grid is given in table 4.1 The grid of straight leading edge diffuser at the leading edge region is shown in figure 4-6 and that of the parabolic leading edge case is shown in figure 4-7. The two grids are smooth and the cells have reasonable aspect ratio. The maximum aspect ratio of the cell is about 10 near the exit. At the entrance region of the diffuser, however, the grid is rather skew (the grid lines intersect each other at 70 deg.). This is unavoidable for a H-type grid [28] in the present vanes orientation. A numerical diagnostic test will be carried out in chapter 5 to check if the skewness of the grid will give rise to any disastrous error.

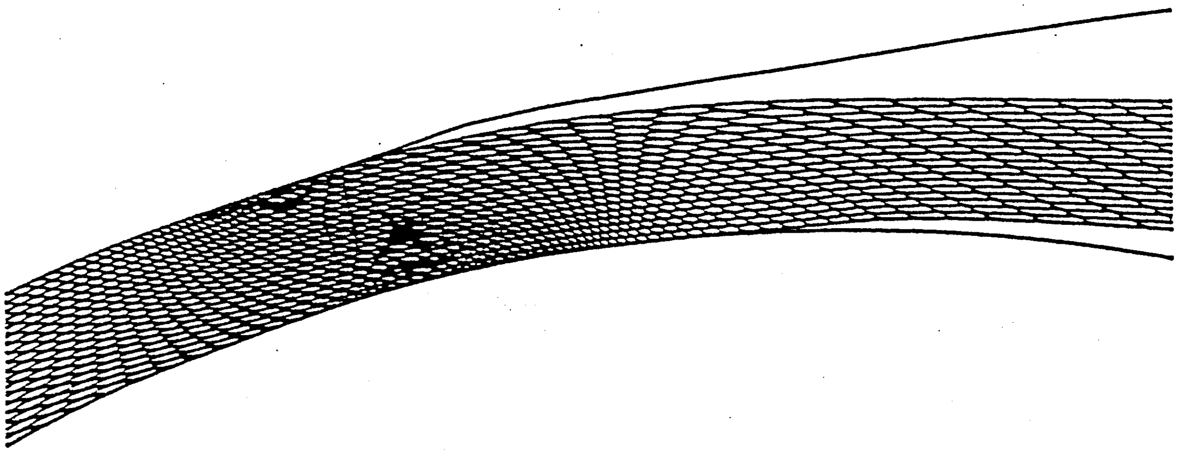

Figure 4-6: The leading edge region of the diffuser with straight leading edge and parallel end walls

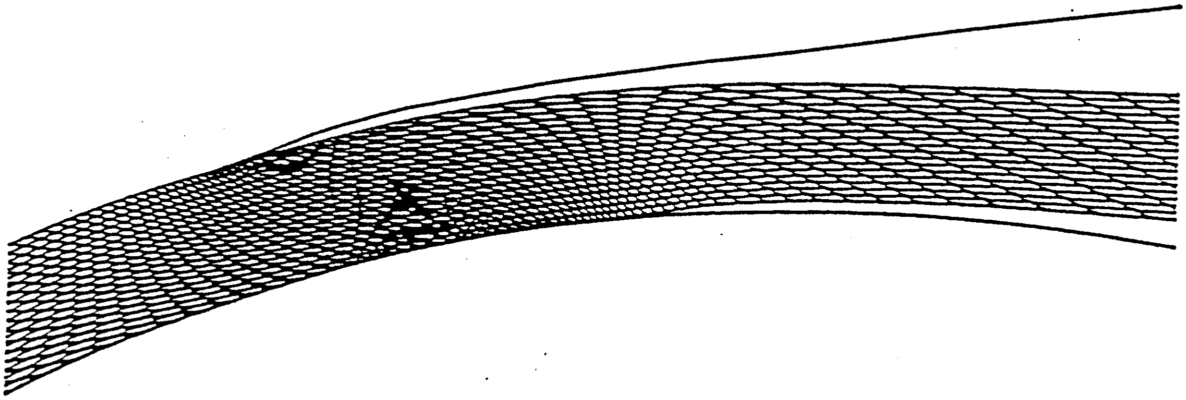

Figure 4-7: The leading edge region of the diffuser with parabolic leading edge and parallel end walls

Chapter 5

Diagnostic Test

5.1 Introduction

The 3-D inviscid computer code used in the present investigation has been shown to be reliable and accurate in computing inviscid flow in axial turbomachines [19]. However, it has not been used in computing flow in radial diffusers of type of interest here. In this chapter, results from diagnostic calculations are presented to demonstrate the adequacy of the computer code for the present application.

A two dimensional spiral flow is chosen to be the test case. An analytical solution can be obtained [29] and the resulting flow field bears similarity to the flow in the diffuser configurations described in chapter 2. A transonic spiral flow field can be computed using this analytical technique. In an inviscid flow, the streamsurface can be replaced by a solid surface without changing the flow field. In the diagnostic test, we choose two adjacent streamlines and impose solid boundary condition from a chosen radial location (this might be, for instance, the inlet of a diffuser of interest here) to the exit. This is equivalent to the calculation of a vaned diffuser with zero thickness vanes. As the solid surfaces coincide with the streamlines, the flow pattern should be the same as that of the flow without solid surfaces. The computed results are then compared with the analytical solution obtained in [29].

5.2 An axisymmetric compressible spiral flow

An axisymmetric spiral flow may be formed from a combination of a vortex flow and a radial flow. A typical streamline pattern in such a flow configuration may be found in [29]. For the sake of completeness and convenience, we will present the analytical solution here. Using polar coordinates, the equations are:
for a flow with a source at the origin

$$2\pi r\rho v_r = \sigma\rho_0 = \text{constant} \tag{5.1}$$

for a flow associated with the potential vortex

$$2\pi r v_\theta = \kappa = \text{constant} \tag{5.2}$$

$$1/2(v_\theta^2 + v_r^2) = c_p T_0[1 - (\frac{\rho}{\rho_0})^{\gamma-1}] \tag{5.3}$$

Upon using $2c_pT_0 = q_{max}^2$ and combining eqn.(5.1) , eqn.(5.2) and eqn.(5.3), we arrive at

$$r^2 = \frac{1}{4\pi^2 q_{max}^2} \frac{\kappa^2(\frac{\rho}{\rho_0})^2 + \sigma^2}{(\frac{\rho}{\rho_0})^2[1 - (\frac{\rho}{\rho_0})^{\gamma-1}]} \tag{5.4}$$

Streamlines for this flow can be most conveniently computed by using a stream-function ψ given as:

$$\frac{1}{r}\frac{\partial\psi}{\partial\theta} = \frac{\rho}{\rho_0}v_r = \frac{\sigma}{2\pi r} \tag{5.5}$$

$$\frac{\partial\psi}{\partial r} = -\frac{\rho}{\rho_0}v_\theta = -\frac{\kappa\frac{\rho}{\rho_0}}{2\pi r} \tag{5.6}$$

Upon introducing a variable A defined as

$$A = \frac{a}{a_0}$$

we can show that

$$\frac{\rho}{\rho_0} = A^{\frac{2}{\gamma-1}} = A^5$$

We can now rewrite eqn.(5.4) in terms of A to give

$$r^2 = \frac{1}{4\pi^2 q_{max}^2} \frac{\kappa^2 A^{10} + \sigma^2}{A^{10}[1 - A^2]} \tag{5.7}$$

Upon differentiating eqn.(5.7), we have

$$\frac{dr}{r} = \left\{ \frac{A^2}{1 - A^2} - \frac{5\sigma^2}{\kappa^2 A^{10} + \sigma^2} \right\} \frac{dA}{A} \tag{5.8}$$

The use of eqn.(5.8) in eqn.(5.6) yields

$$d\psi = -\frac{\kappa}{2\pi} \left\{ \frac{A^6}{1 - A^2} - \frac{5\sigma^2 A^4}{\kappa^2 A^{10} + \sigma^2} \right\} dA \tag{5.9}$$

which, upon integration, results in

$$\psi = \frac{\kappa}{2\pi} \left\{ \frac{\sigma}{\kappa} \arctan \frac{\kappa A^5}{\sigma} - \frac{1}{2} \ln \frac{1+A}{1-A} + A + \frac{1}{3}A^3 + \frac{1}{5}A^5 \right\} + f(\theta) \tag{5.10}$$

However eqn.(5.5) can be integrated to give

$$\psi = \frac{\sigma\theta}{2\pi} + g(r) \tag{5.11}$$

Thus from eqn.(5.10) and eqn.(5.11), we can identify

$$f(\theta) = \frac{\sigma\theta}{2\pi}$$

so that ψ is given by

$$2\pi\psi = \sigma \left\{ \theta + \arctan \frac{\kappa A^5}{\sigma} \right\} - \kappa \left\{ \frac{1}{2} \ln \left(\frac{1+A}{1-A} \right) - A - \frac{1}{3}A^3 - \frac{1}{5}A^5 \right\} \tag{5.12}$$

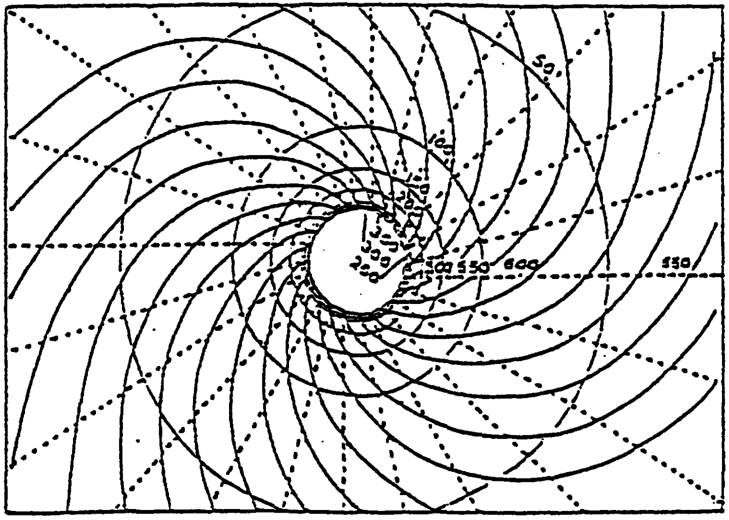

Figure 5-1: Streamline of spiral flow

The results in eqn.(5.7) and eqn.(5.12) can now be used to compute the streamline pattern for this simple flow. Since altering the value of ψ is equivalent to altering the value of θ, all streamlines have the same shape. Fig. 5-1 (from [29]) shows the complete streamlines as determined from equations (5.7) and (5.12).

5.3 Computational results

In this section we present results to demonstrate that the computer code yields results that agree with the analytical solution. It should be noted here that we are using a three-dimensional Euler code to compute a two-dimensional flow. The two dimensional grid in $r - \theta$ plane is shown in fig. 5-2. The three dimensional grid is constructed by stacking the two dimensional grids in the z direction. The swirl angle at the inflow is 69 deg. The exit pressure is the same as that calculated from the theory in the previous section. Fig. 5-3 shows the pressure distribution calculated from the code while fig. 5-4 shows the pressure distribution from the theory. It can be seen that the computed results agree

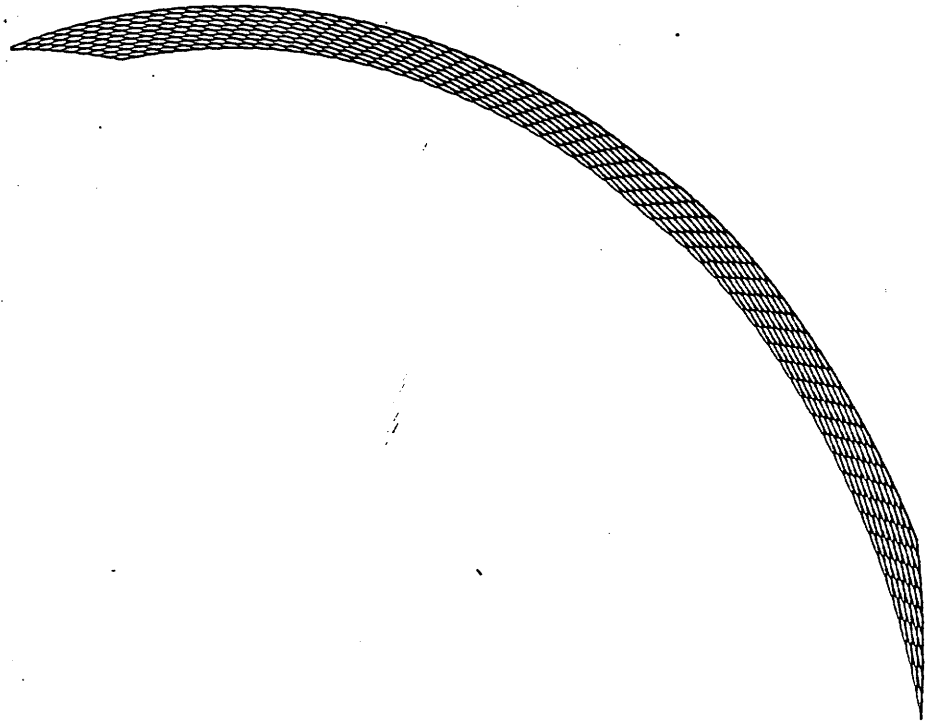

Figure 5-2: Computational grid of test case, $r - \theta$ plane

very well with the analytical solution. The largest difference between the two pressure field occurs at the leading edge region; the maximum difference being less than 5%. Such a difference is due to a change in boundary condition from periodic boundary condition to that of solid surface boundary condition at the leading edge. The error is acceptable in the present investigation because it only affects the flow field locally. The difference between the two pressure fields becomes negligible after several grid points downstream the leading edge.

5.4 Concluding remark

We have shown that the computational results agree favorably with the analytical solution. Some errors can be seen in the leading edge region. In the test case, the angle of incidence is 0 deg. The leading edge error may become more severe when the angle of incidence becomes larger. Apparently, the skewness of the grid does not result in significant errors. The modification of the computer code in inflow and outflow conditions gives satisfactory results in the two dimensional flow test case. The diagnostic test case provides a simple way to verify the correctness of the modification. The code is three dimensional and it has been tested thoroughly by Adamczyk et al [19] in three dimensional flow. No test case has been done in the present investigation to verify its correctness in three-dimensional applications. This diagnostic test serves to demonstrate the validity of the use of this code for computing flow in a flow configuration representative of a radial diffuser.

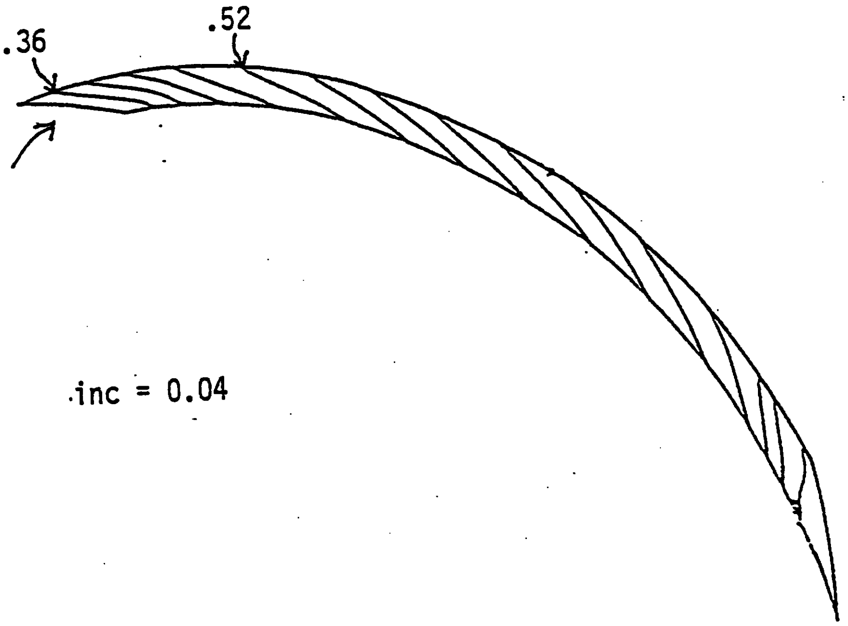

Figure 5-3: Computed presure distribution

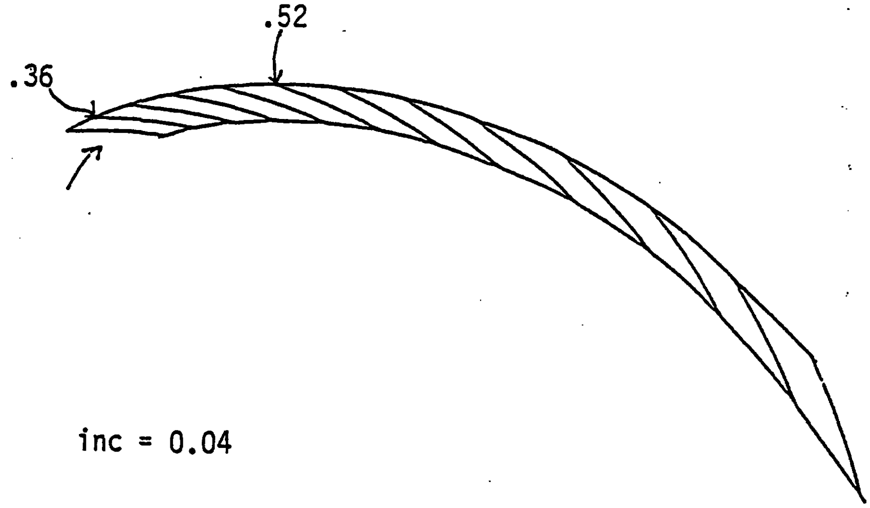

Figure 5-4: Pressure distribution from analytical solution

Chapter 6

Results and discussion

6.1 Introduction

An analysis of the computed flow fields for four different diffuser configurations will be presented. The geometrical configuration for these four diffusers will be described in the following. An inviscid flow model is assumed and all the calculations have been implemented using the inviscid Euler code alluded in the previous chapter. The diffuser inlet conditions are assumed to be uniform in axial and tangential directions. Pressure recovery and changes in entropy will be used to assess the influence of Campbell diffuser.

The four diffusers configurations being investigated are as follows:

1. A straight vane leading edge with parallel end walls.
2. A straight vane leading edge with non-axisymmetric end walls.
3. A parabolic vane leading edge with parallel end walls.
4. A parabolic vane leading edge with non-axisymmetric end walls.

The characteristic geometrical parameters are delineated in Table 2.1 in chapter 2. These four diffuser configurations will serve as the baseline calculations. Additional calculations based on variations of these four baseline diffuser configurations have also been carried out. These additional calculations are used to interpret findings in the baseline calculations. Details of the additional calculations will be given after the presentation of results from the baseline calculations.

6.2 Velocity field and streamwise pressure gradient

Figures 6-1 and 6-2 show the velocity fields at midspan around the leading edge region of the diffuser with straight vane leading edge and parallel end walls and that with straight vane leading edge and non-axisymmetric end walls . It can be seen that the flow enter the blade surface at about 5 deg. incidence at the pressure side. After a short distance downstream from the leading edge, the velocity appears to follow the diffuser passage. Figures 6-3 and 6-4 show the velocity field in the throat region on $z - \theta$ plane. In these figures, the velocity vectors are projected on the $z - \theta$ plane of radial location of the throat. These show that the axial velocity (z- component) is much smaller than the absolute velocity, as one would have expected from the specified diffuser geometrical configurations.

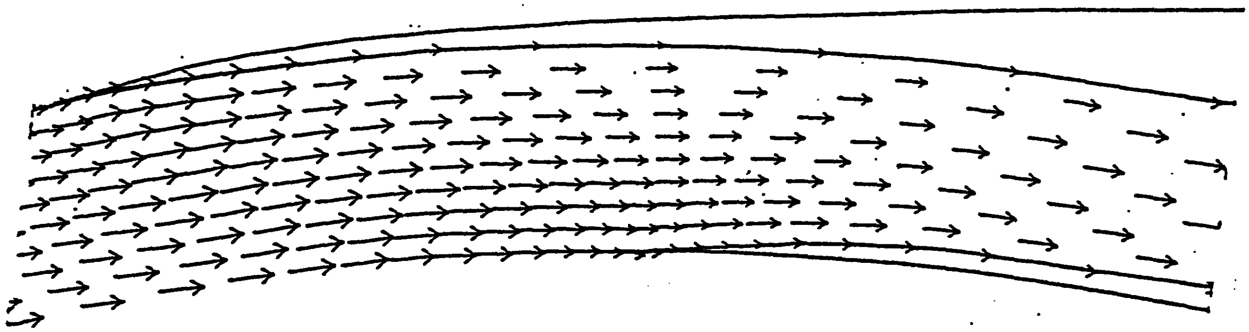

Figure 6-1: Velocity field at midspan around leading edge region of the diffuser with straight vane leading edge and parallel end walls

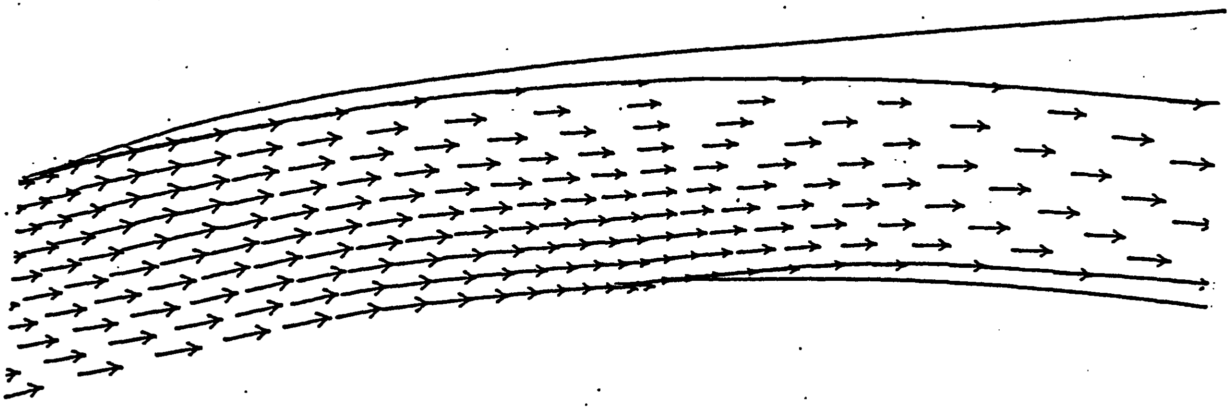

Figure 6-2: Velocity field at midspan around leading edge region of the diffuser with straight leading edge and non-axisymmetric end walls

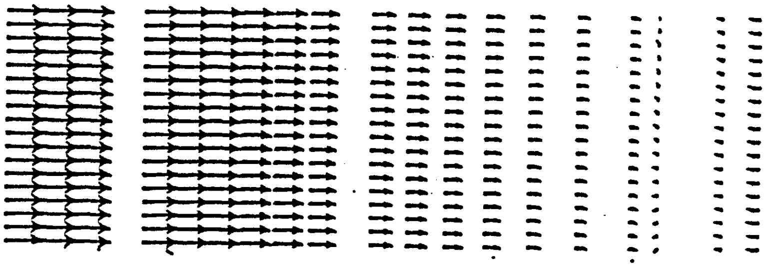

Figure 6-3: Velocity at the throat in $z - \theta$ plane of the diffuser with straight leading edge and parallel end walls

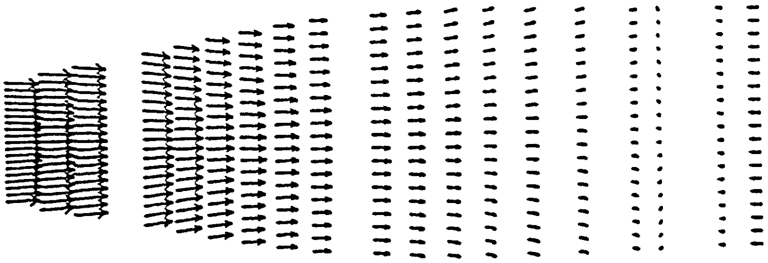

Figure 6-4: Velocity at the throat in $z - \theta$ plane of the diffuser with straight leading edge and non-axisymmetric end walls

Figures 6-5 and 6-6 show the streamwise pressure gradient($\vec{v} \cdot \nabla P/|\vec{v}|$) on the end wall of the diffuser with straight vane leading edge and parallel end walls and that with straight vane leading edge and non-axisymmetric end walls respectively. A large magnitude of streamwise pressure gradient is observed near the leading edge. The rapid change in flow direction to follow the solid boundary gives rise to the rapid change in pressure gradient in that region. Upon comparing the computed results, it appears that the flow entering the diffuser more smoothly in the non-axisymmetric end walls diffuser. There is a higher adverse pressure gradient between the two blades in the parallel end wall diffuser. Converging the pressure side passage depth helps the flow to follow the pressure side at the diffuser entry. However, we have to pay the price at the suction side. In order to keep the one-dimensional area distribution the same in two cases, the suction side passage width must be diverging. The concave shape of the end wall has a less favorable pressure gradient than that in the parallel end walls diffuser.

The velocity field and the streamwise pressure gradient field shown in this section are to be expected. They serve a diagnostic purpose to show that the computer code yields reasonable results.

6.3 Straight leading edge vaned diffusers

The Mach number distribution of the two diffusers at mid-span in the vaneless and semi-vaneless space are shown in figure 6-7 and figure 6-8.

Only three passages are shown in the figures. In the centrifugal diffuser, there should be 31 passages, but the three passages shown here should be enough to illustrate the periodicity in the circumferential direction. The Mach number distribution indicates that there is a bow shock upstream of the throat. Similar results have been obtained by Colantuoni et al. [12]. Figure 6-9 shows a sketch of Mach number distribution deduced from the computed results. Only three Mach lines are shown to illustrated the formation of bow shock. The Mach number changes from 1.2 to a subsonic value in the region

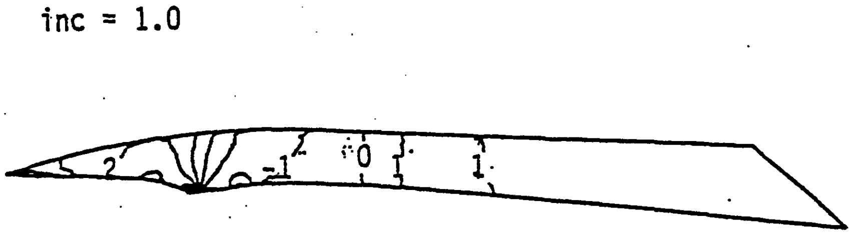

Figure 6-5: Streamwise pressure gradient on end wall of the diffuser with straight leading edge and parallel end walls

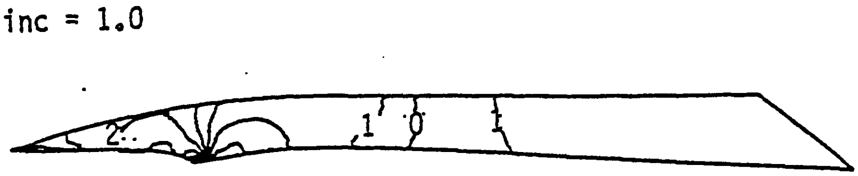

Figure 6-6: Streamwise pressure gradient on end wall of the diffuser with straight leading edge and non-axisymmetric end walls

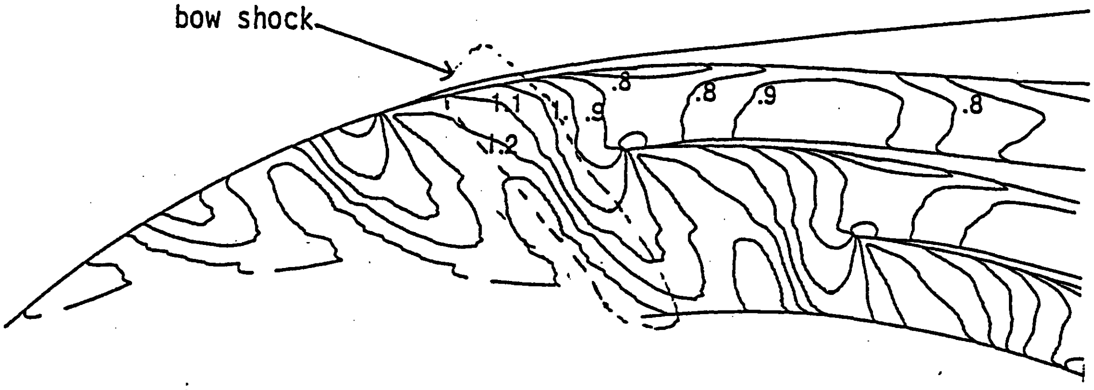

Figure 6-7: Mach number distribution at mid-span of the straight leading edge parallel end walls diffuser

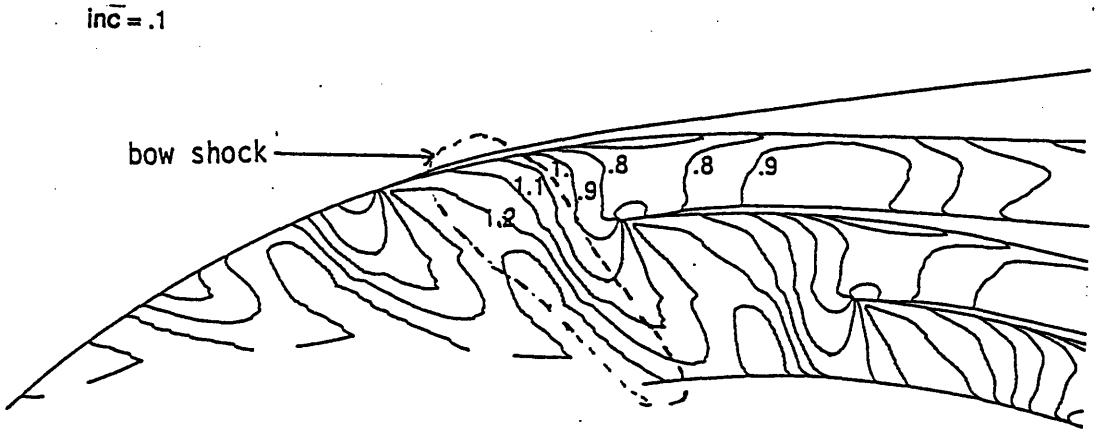

Figure 6-8: Mach number distribution at mid-span of the straight leading edge non-axisymmetric end walls diffuser

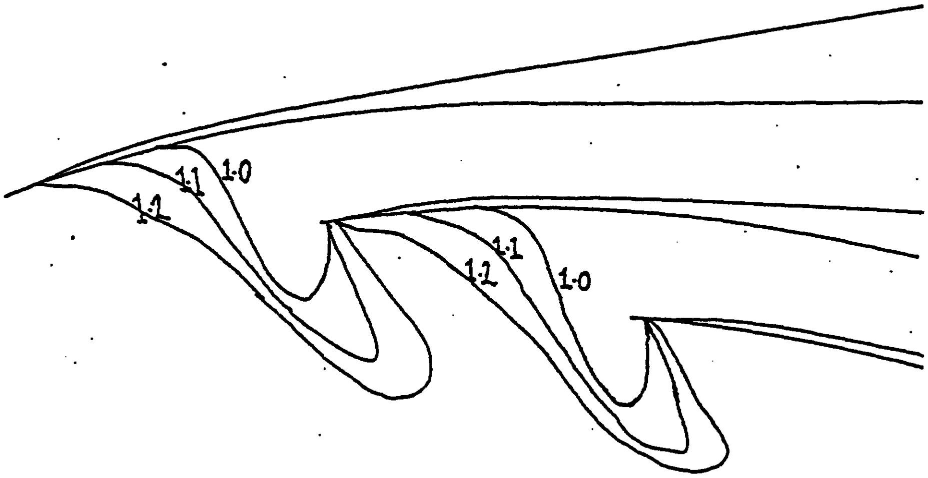

Figure 6-9: Sketch of the Mach number distribution to illustrate the bow shock region

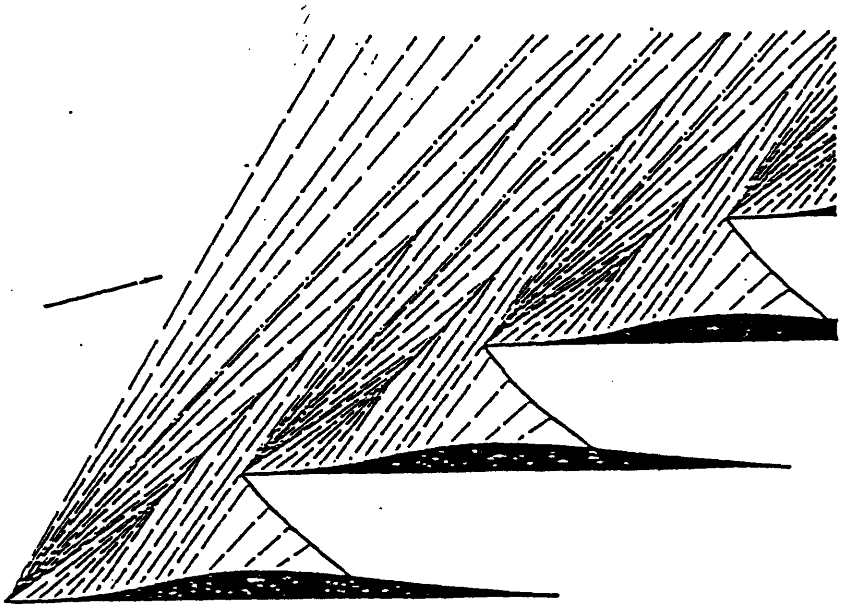

Figure 6-10: cascade at subsonic radial inlet flow Mach number

upstream of the leading edge suggesting that there is a bow shock. The formation of this bow shock will be explained in the following.

Lichtfuss and Starken gave a comprehensive account of the difference between a cascade and a single profile in supersonic flow [30]. Figure 6-10 shows a radial cascade with a subsonic radial inlet flow Mach number. For a radial cascade, there are infinitely many blades in front of each blade. Since the radial component is subsonic, the disturbance can extend in the radial direction upstream. The entire flow area upstream of the cascade inlet is then covered by Mach lines. The Mach lines extend upstream to infinity and therefore are able to influence the inlet flow presumed to be there. As shown in figure 6-10, the concave shape of the suction side results in the convergence of the Mach lines emanating from the surface to form a shock i.e. the characteristics coming from the blade contour form an envelope, at the cusp of which an oblique shock wave starts [31].

In figures 6-7 and 6-8 we can see a similar merging of the Mach lines starting from the concave suction side and conclude that there is a bow shock in the flow.

6.3.1 Pressure distribution

The pressure distribution at midspan of the parallel end walls diffuser and that of the non-axisymmetric end walls diffuser are shown in figure 6-11 and figure 6-12. Firstly, we notice that the pressure contour does not bear the similarity to the Mach number contour as one might have anticipated in an inviscid isentropic flow; this feature of the comparison between the computed pressure contour and the computed Mach number contour can be clearly seen near the solid boundary. This is due to the entropy generated at the leading edge by the inherent artificial viscosity used in the Euler code [19]. Because of this, we argue that it is far more appropriate to use the pressure field as a better representation of the flow field than that given in term of Mach number. From now on, only the pressure field is used for the investigation. There is no much difference between the two cases in the semi-vaneless region shown in figures 6-11 and 6-12. Figure 6-13 and figure 6-14 show the pressure distribution at hub and shroud of the non-axisymmetric diffuser respectively.

The computed results show that the shock, which is located in the semi-vaneless region, is not affected by the contouring of end wall in the channel diffuser region. It can be observed that the variation in flow field from one end wall to another is quite negligible. (comparing fig. 6-12, fig. 6-13 and fig. 6-14).

Figure 6-15 and figure 6-16 show the isobars on the blade surfaces and midstream meridional plane of the parallel end walls diffuser and the non-axisymmetric diffuser respectively. The suction side reacceleration is less significant in the non-axisymmetric diffuser. In a diffuser, reacceleration of flow is undesirable, and should be minimized for better performance. The spacing of the isobars of the parallel end walls diffuser is closer than that of the non-axisymmetric end walls diffuser suggesting that there is a sharper change in pressure gradient in the parallel end walls diffuser. Large adverse pressure gradient at the entrance may cause flow separation in that region.

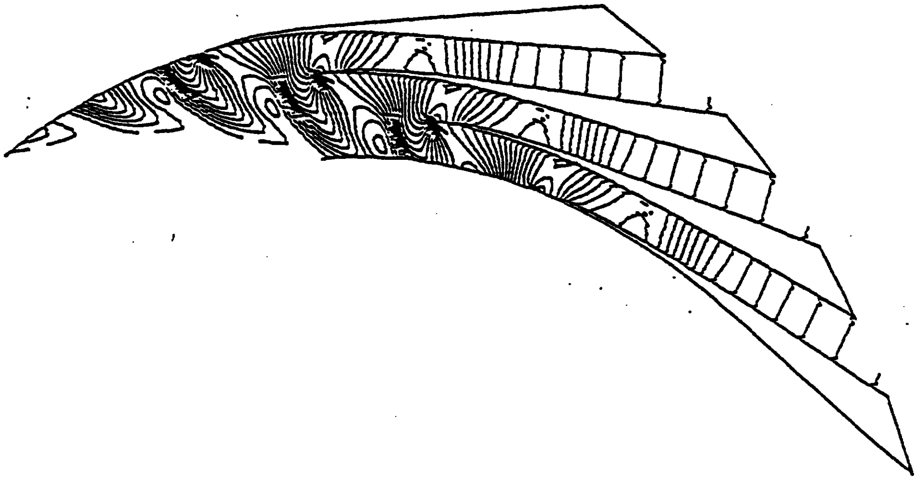

Figure 6-11: Pressure distribution at midspan of the diffuser with straight leading edge and parallel end walls

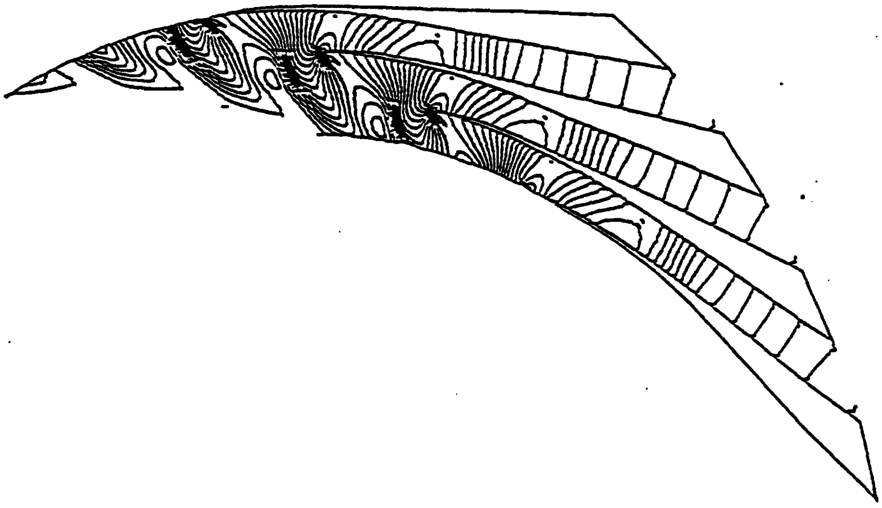

Figure 6-12: Pressure distribution at midspan of the diffuser with straight leading edge and non-axisymmetric end walls

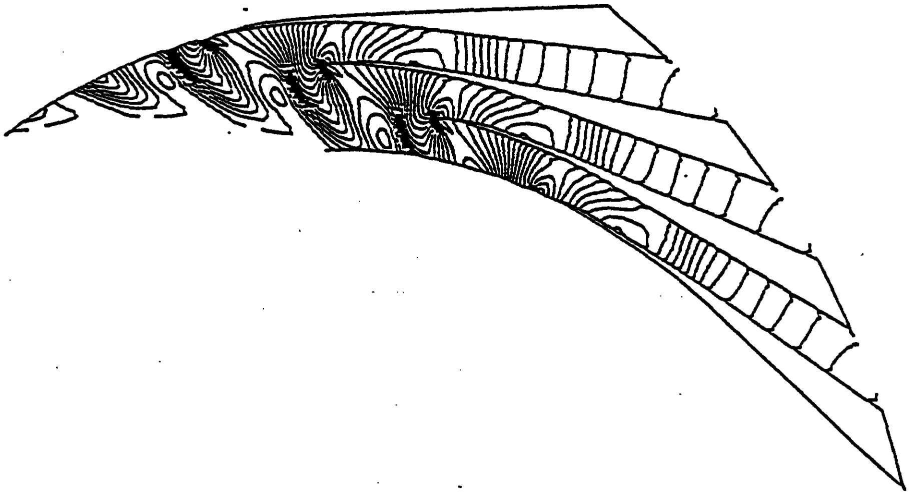

Figure 6-13: Pressure distribution at hub of the diffuser with straight leading edge and non-axisymmetric end walls

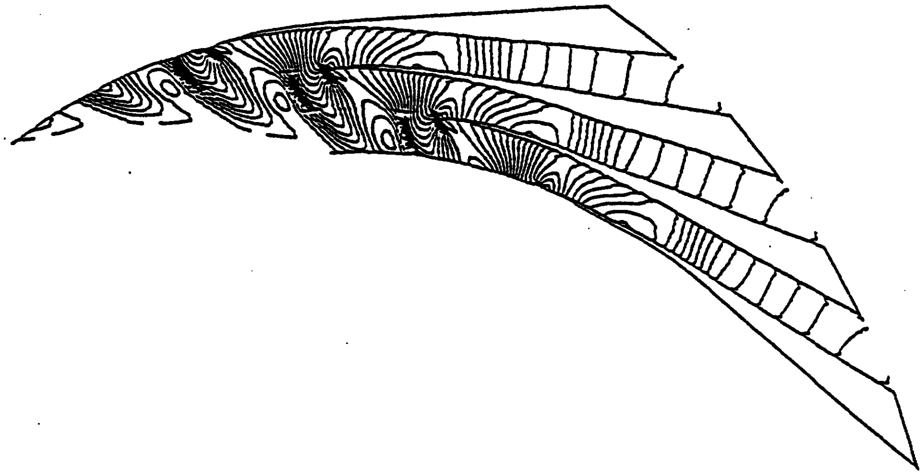

Figure 6-14: Pressure distribution at shroud of the diffuser with straight leading edge and non-axisymmetric end walls

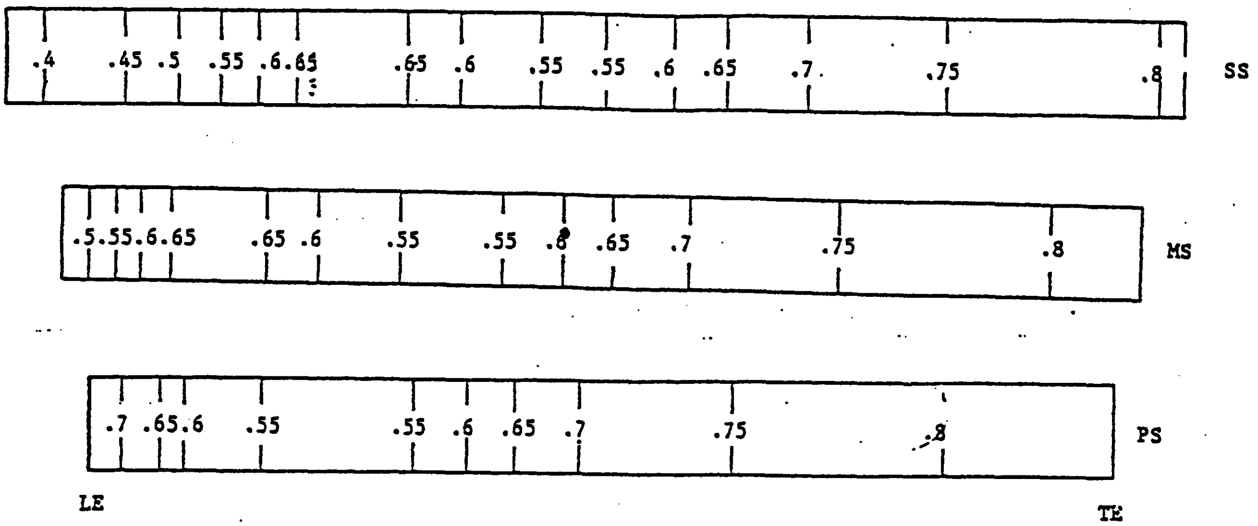

Figure 6-15: Pressure distribution on blade surfaces and midstream meridional of the diffuser with straight leading edge and parallel end walls

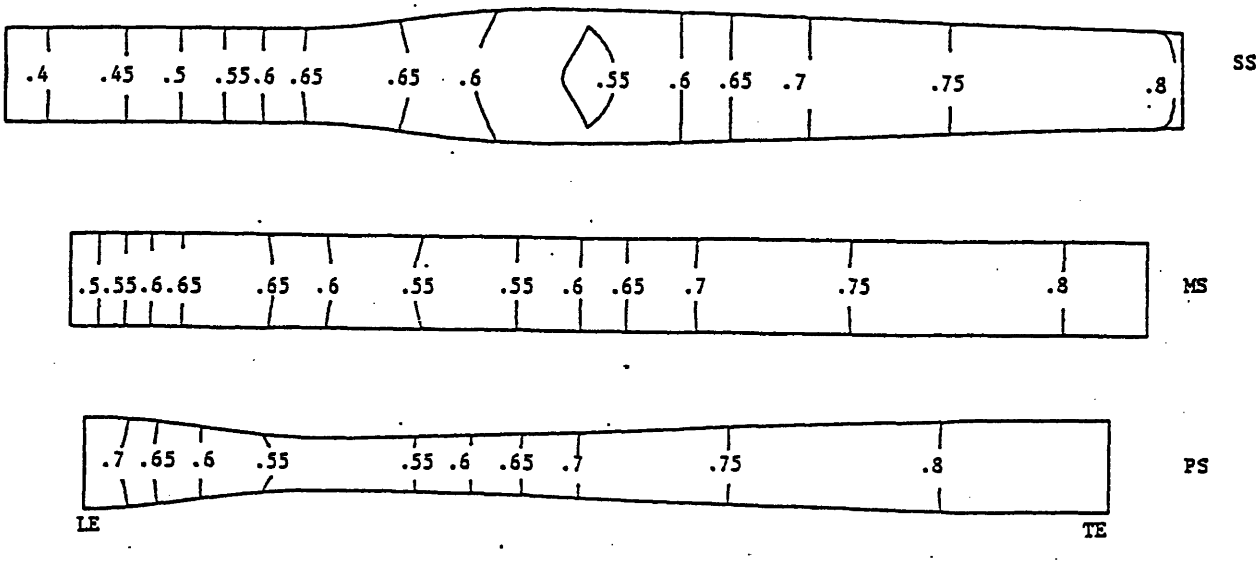

Figure 6-16: Pressure distribution on blade surfaces and midstream meridional of the diffuser with straight leading edge and non-axisymmetric end walls diffuser

6.3.2 Pressure recovery

Pressure recovery is an important factor to consider when designing a diffuser. The overall pressure discovery is defined as

$$c_{pD} = \frac{\bar{P}_4 - \bar{P}_2}{\bar{P}_{02} - \bar{P}_2} \tag{6.1}$$

where $^-$ denotes the mass average of the quantity. The c_{pD} of the parallel end walls diffuser is 0.83 while that of the non-axisymmetric end walls diffuser is 0.84. Figure 6-17 shows pressure recovery along the radial distance in two cases. The difference in pressure recovery between the Campbell diffuser and the two-dimensional diffuser is negligible.

6.3.3 Stagnation pressure loss and entropy

The stagnation pressure loss of the two cases is rather high. It is about 5% in both cases. This value is higher than the change in stagnation pressure across an assumed normal shock corresponding to a Mach number of 1.2. Dolan and Runstadker[32] reported such a problem in 1979 and also Osborne and Japikse [33] thereafter. Data covering this loss is extremely limited. The computational results is further deteriorated by the artificial viscosity. In figure 6-18, it can be seen that the entropy is generated at the leading edge and is being convected downstream. The production of entropy is due to the finite incidence of the flow at the blade leading edge. The flow is constrained to follow the solid boundary. This will create a high pressure gradient locally which in turn switch on the second order smoothing. The smoothing term produces entropy and non-physical stagnation pressure loss. Since the two cases are subjected to identical conditions, so that comparison of entropy can still be used to assess the performance of the diffuser.

Figure 6-20 and 6-21 shows the stagnation pressure loss of straight leading edge diffusers at midspan. Before the diffuser throat, there is a significant loss. The mass average of the stagnation pressure of the two cases are plotted along the radial distance from inlet to the leading edge in figure 6-22. From this plot, we can compare the loss

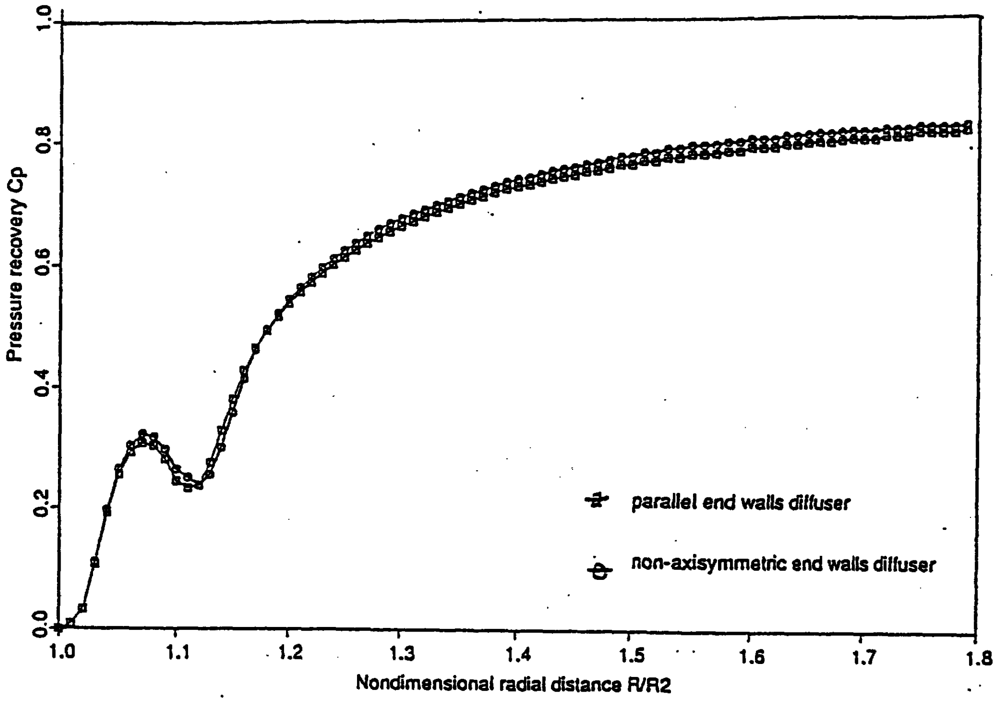

Figure 6-17: Pressure recovery of diffusers with straight vane leading edge

from inlet to the leading edge in figure 6-22. From this plot, we can compare the loss of stagnation pressure due to the shock. The stagnation pressure loss of the diffuser with parallel end walls obtained from the computed results is 2.9% while that of the diffuser with non-axisymmetric end walls is 3.2%. The entropy contours of the two cases at midspan are shown in figure 6-18 and 6-19. Figure 6-23 show the stagnation pressure loss of the non-axisymmetric diffuser at the hub. It is very similar as that at the midspan. This is expected since variation of flow field in axial direction appears to be negligible.

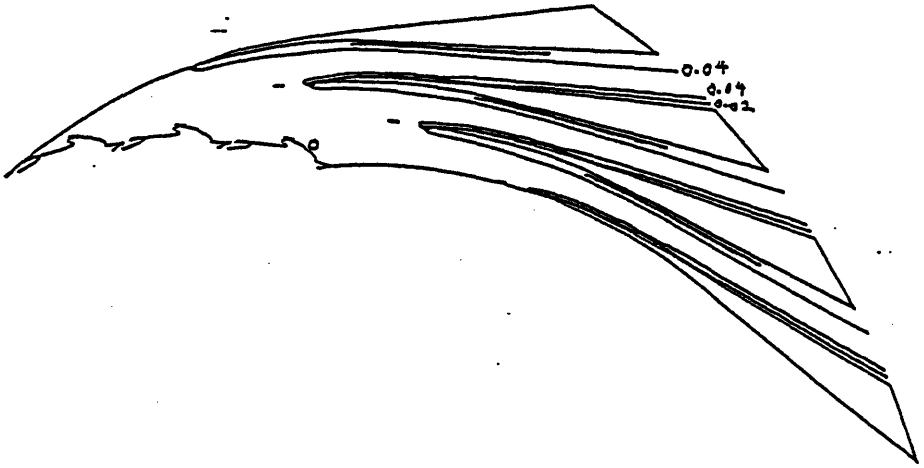

Figure 6-18: Entropy at midspan of the diffuser with straight leading edge and parallel end walls

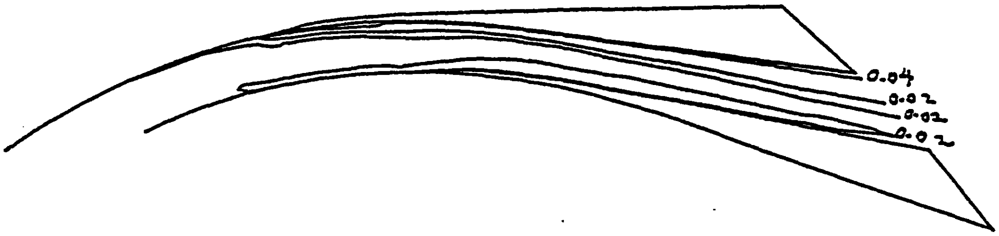

Figure 6-19: Entropy at midspan of the diffuser with straight leading edge and non-axisymmetric end walls diffuser

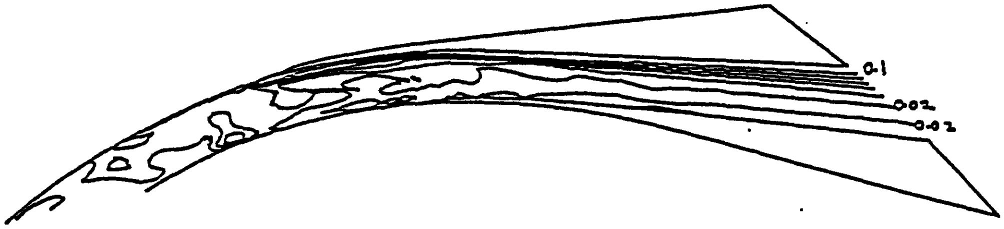

Figure 6-20: Stagnation pressure loss at midspan of the diffuser with straight leading edge and parallel end walls

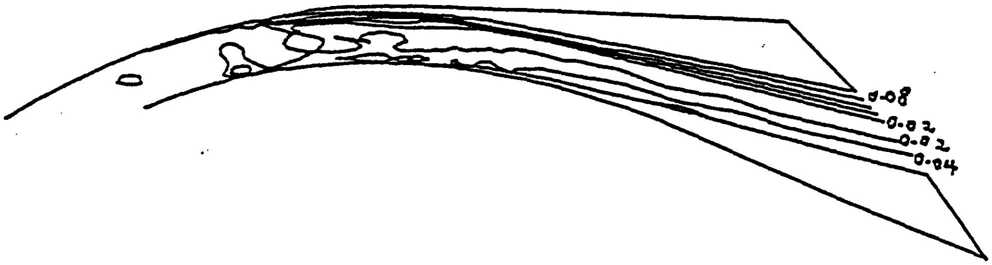

Figure 6-21: Stagnation pressure loss at midspan of the diffuser with straight leading edge and non-axisymmetric end walls

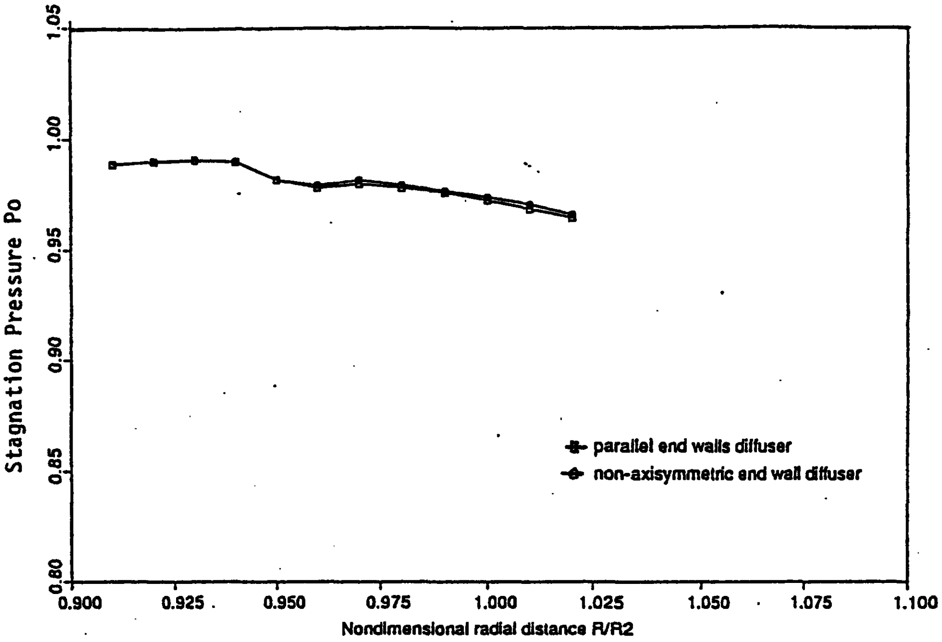

Figure 6-22: Mass average stagnation pressure of diffusers with straight leading edge

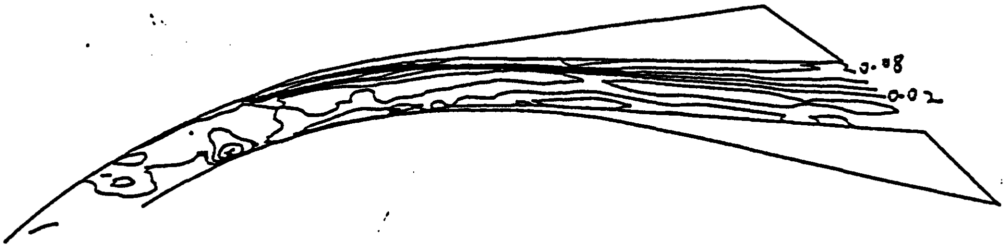

Figure 6-23: Stagnation pressure loss at hub of the diffuser with straight leading edge and non-axisymmetric end walls

6.4 Parabolic leading edge vaned diffusers

In this section similar results from the calculations with the straight leading edge vane replaced by parabolic leading edge vane will be presented to illustrate the influence of the resulting end wall contouring on the computed flow fields. As in the case with straight leading edge vaned diffusers, it will be seen that the parabolic leading edge vaned diffusers with parallel end walls and that with non-axisymmetric end walls have similar flow fields.

6.4.1 Pressure distribution

The pressure distribution at midspan of the parallel end walls diffuser and the non-axisymmetric end walls diffuser are shown in figure 6-24 and figure 6-25 respectively. Again there is no much difference between the two cases. Figure 6-26 and figure 6-27 show the pressure distribution at hub and shroud of the non-axisymmetric end walls diffuser respectively. Figure 6-28 and figure 6-29 show isobars on the blade surfaces and midspan meridional plane of the two diffusers respectively. From these it can be observed that the flow field from one end wall to another is quite negligible.

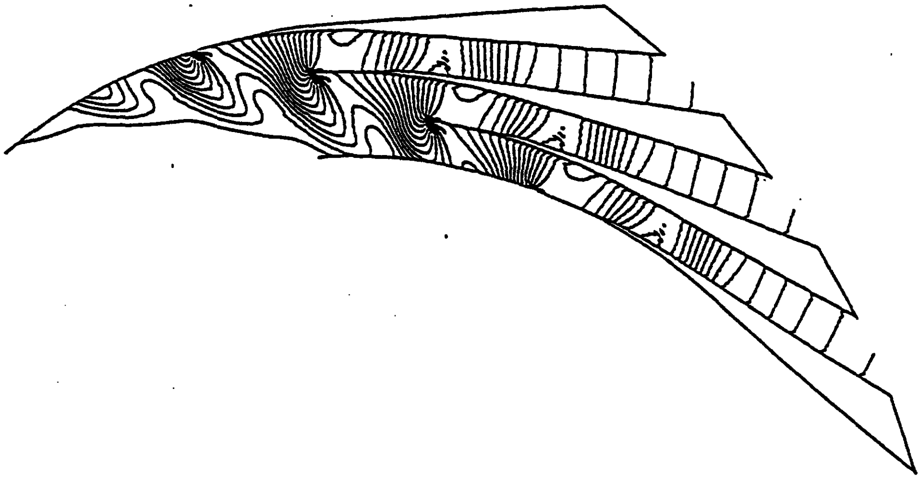

Figure 6-24: Pressure distribution at midspan of the diffuser with parabolic leading edge and parallel end walls

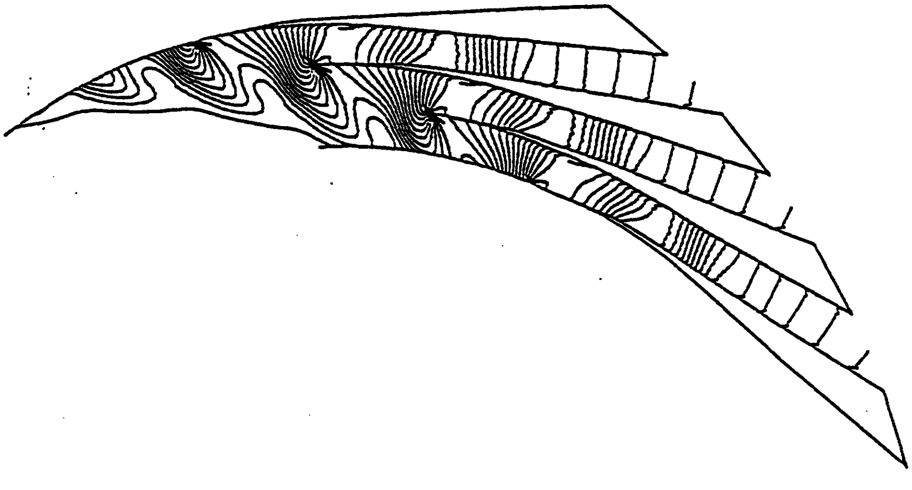

Figure 6-25: Pressure distribution at midspan of the diffuser with parabolic leading edge and non-axisymmetric end walls

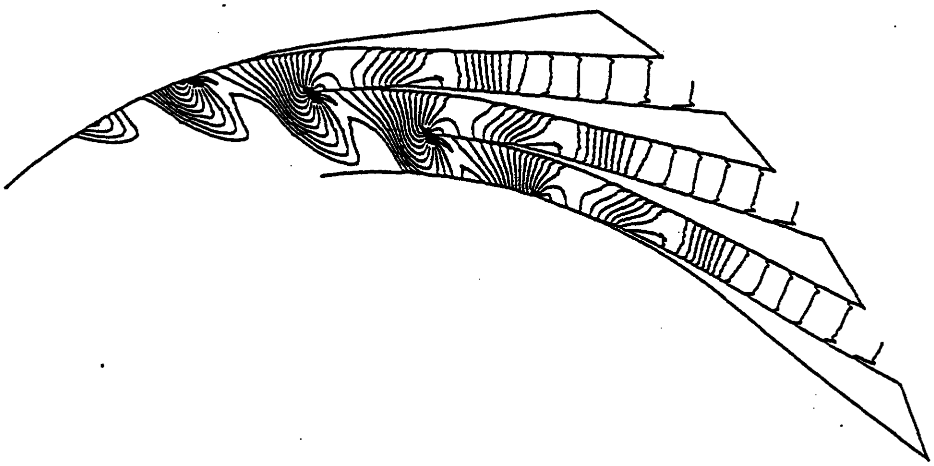

Figure 6-26: Pressure distribution at hub of the diffuser with parabolic leading edge and non-axisymmetric end walls

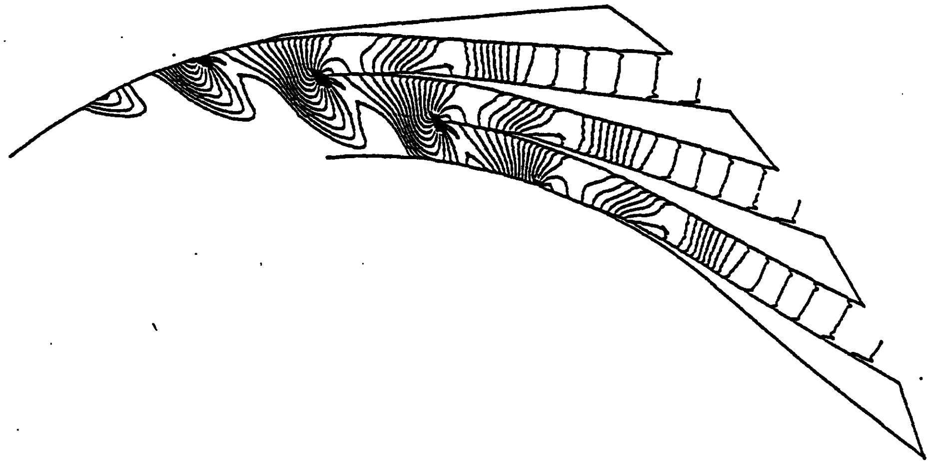

Figure 6-27: Pressure distribution at shroud of the diffuser with parabolic leading edge and non-axisymmetric end walls

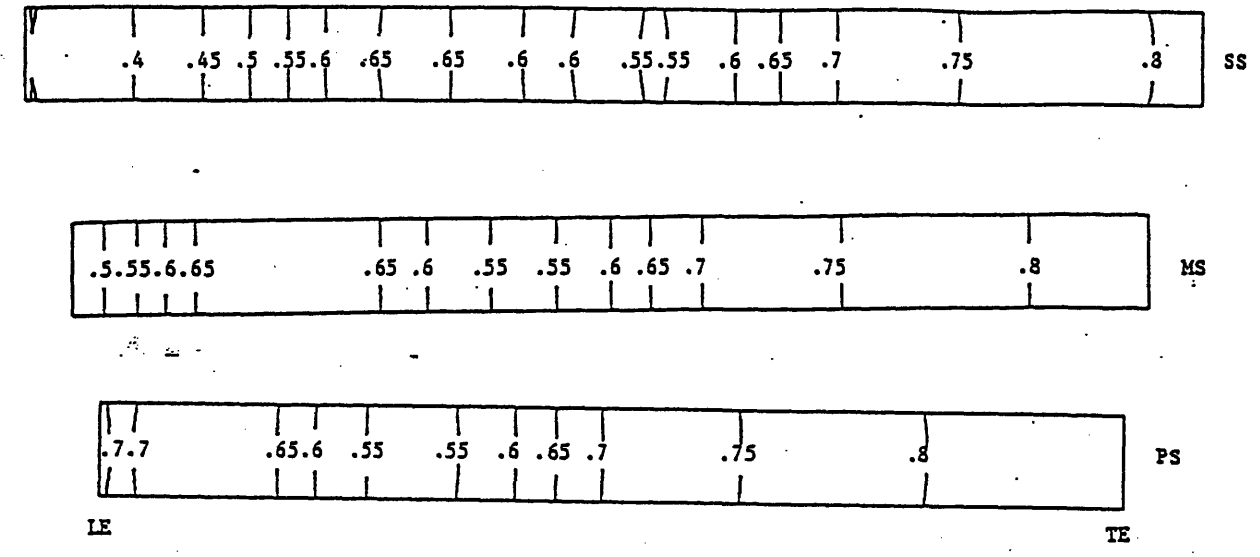

Figure 6-28: Pressure distribution on blade surfaces and midstream meridional plane of the diffuser with parabolic leading edge parallel end walls

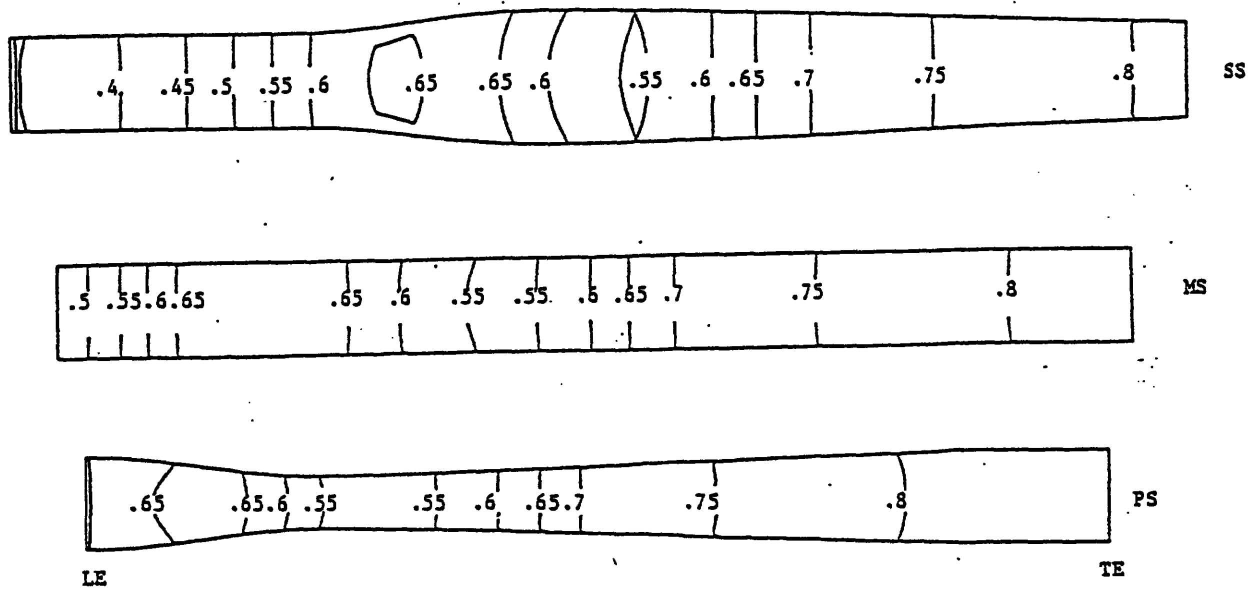

Figure 6-29: Pressure distribution on blade surfaces and midstream meridional plane of the diffuser with parabolic leading edge and non-axisymmetric end walls

6.4.2 Pressure recovery

The pressure recovery of the diffusers is shown in figure 6-30. The c_{pD} of the parallel end walls diffuser and that of the non-axisymmetric end walls diffuser are the same (0.82). The two curves effectively collapse into one. The less than 0.002 difference in c_p is within computational error.

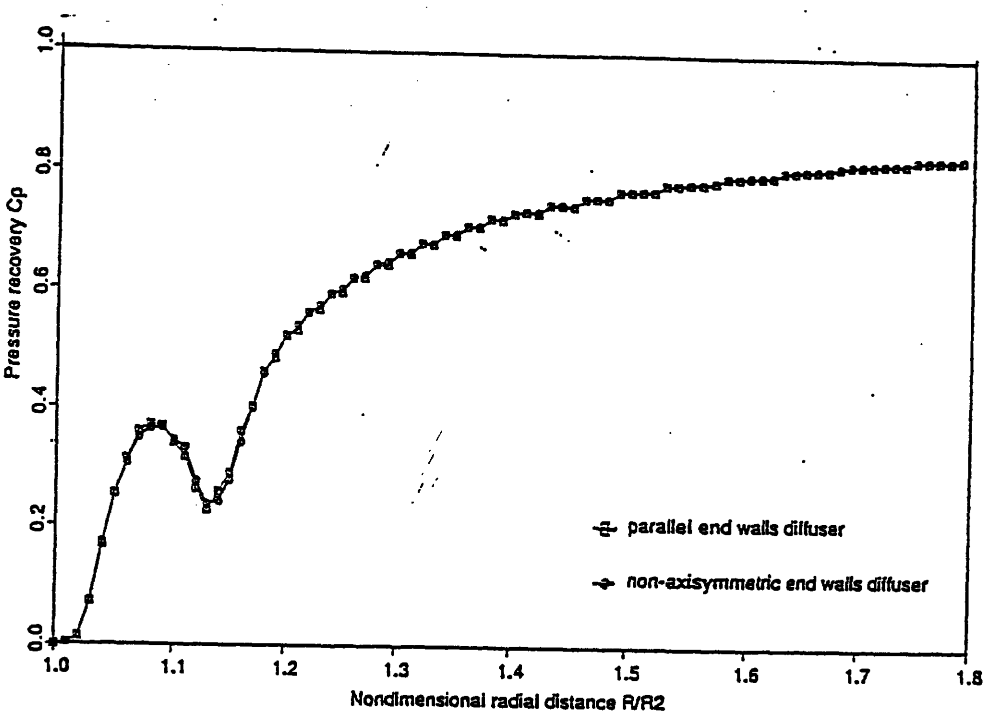

Figure 6-30: Pressure recovery of the diffusers with parabolic leading edge

6.4.3 Stagnation pressure loss and entropy

The stagnation pressure loss of the diffusers with parabolic leading edge is smaller than that of the diffusers with straight leading edge. Figure 6-31 and figure 6-32 show the stagnation pressure loss of the diffuser with parallel end walls at midspan and that of the diffuser with non-axisymmetric end walls at midspan respectively. The stagnation pressure loss due to shock is smaller. Similar entropy generation due to incidence can be seen in figure 6-33 and figure 6-34. Figure 6-35 shows the mass average stagnation pressure along the radial direction from inlet to leading edge. From the computed results, the stagnation pressure loss of the diffuser with parallel end walls is 1.3% while that of the one with non-axisymmetric end walls is 1.5%. It can be seen in both straight leading and parabolic leading edge cases, the Campbell diffusers appear to have about the same stagnation pressure loss. The difference of about .2% in both cases is not sufficient to make a concluding statement on the shock strength by assessing the stagnation pressure loss.

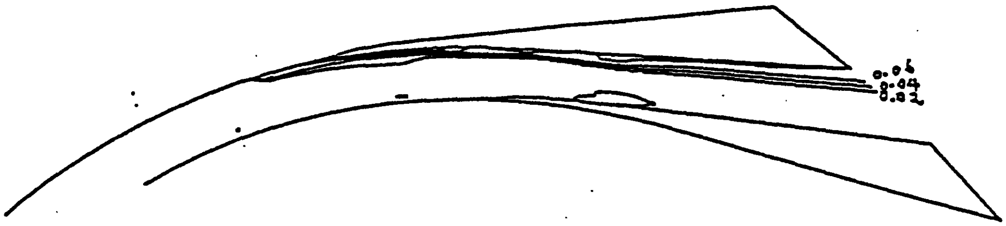

Figure 6-31: Stagnation pressure loss at midspan of the diffuser with parabolic leading edge and parallel end walls

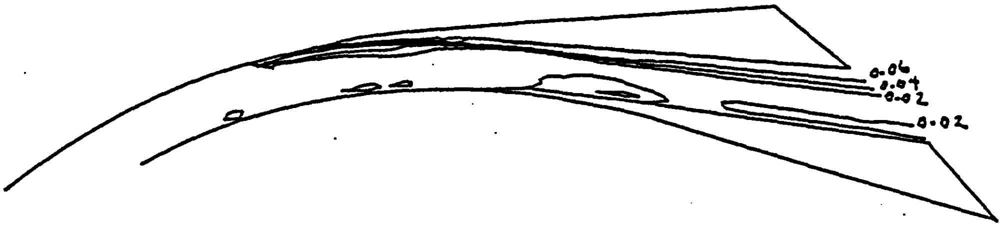

Figure 6-32: Stagnation pressure loss at midspan of the diffuser with parabolic leading edge and non-axisymmetric end walls

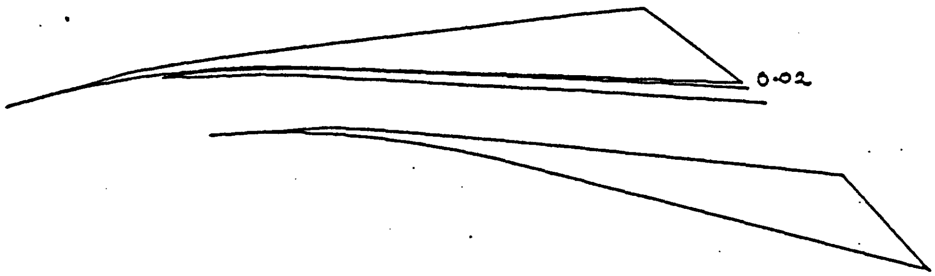

Figure 6-33: Entropy at midspan of the diffuser with parabolic leading edge and parallel end walls

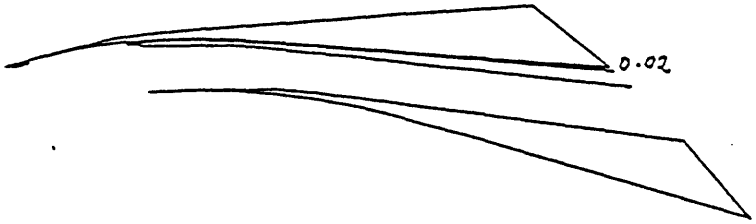

Figure 6-34: Entropy at midspan of the diffuser with parabolic leading edge and non-axisymmetric end walls

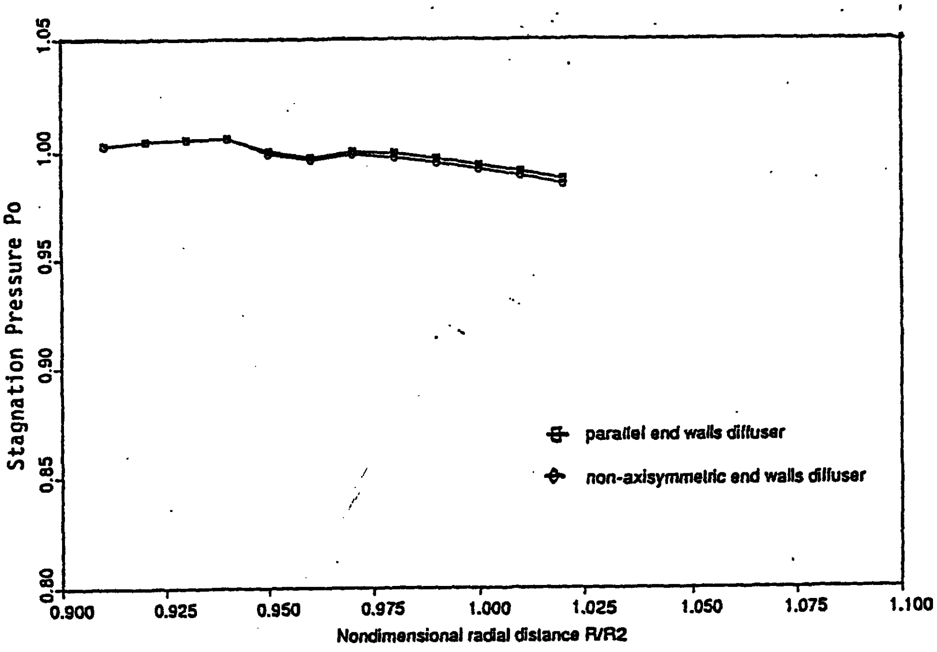

Figure 6-35: Mass average stagnation pressure of diffusers with parabolic leading edge

6.5 Synthesis of observations on computed results

The results of the calculations described in the foregoing sections may be rather surprising at first glance; a change in geometry due to end wall contouring seems to have little effect on the flow field. In these diffuser configurations, the characteristic length scales on the crossflow plane (i.e. the pitch and the distance between the end walls) are small compared to the characteristic length scale in the streamwise direction (i.e. the chord length). Consequently these diffuser passages tend to form narrow flow path to constrain the flow in the passage to remain essentially one dimensional [34]. The introduction of end wall contouring would merely bring about a change in the flow dimension on the crossflow plane so that it is not surprising to find that the resulting change in the flow field is minimal. In an attempt to clarify this particular aspect of the flow field, further parametric calculations are carried out to show the influence of both the ratio of passage depth to chord length (δ/c) and the ratio of pitch to chord (ϵ/c). These will be presented in the next section.

6.6 Further computational investigation

Calculations are implemented to show the influence of δ/c and ϵ/c. The calculations of the previous four diffusers are repeated with the passage depth increased by 2.5 times. The calculations of diffusers with different pitch-to-chord ratio(ϵ/c) have also been carried out. The pitch-to-chord ratio is changed by varying the stagger angle and the number of blades. A straight leading edge vaned diffuser with the same number of blades as the baseline calculation (31 blades) is used in the calculation. The stagger angle is decreased to open up the flow area. The pitch-to-chord ratio is therefore increased. The diffusers with parallel end walls and that with non-axisymmetric end walls are studied at the new stagger angle. Finally, the pitch-to-chord ratio is decreased by increasing the number of blades to 41. It is appropriate to point out that in the parametric calculations to investigate the influence of the pitch-to-chord ratio, the flow passage does not resemble any practical diffusers. The divergence angle of the channel is close to 0 deg. and the profile of the suction side has not been tailored for the new stagger angle. A large incidence angle is expected and separation may possibly occur.

In the following, we present results of two sets of parametric calculations. The first set is to investigate the influence of passage depth to chord ratio on end wall contouring while the second set is to investigate the influence of pitch-to chord ratio.

6.6.1 Investigation of influence of passage depth to chord ratio

To show the influence of passage depth to chord ratio, the following calculations were carried out:

1. same diffuser configuration as the diffuser with straight leading edge and parallel end walls but with its passage depth increased by 2.5 times
2. same diffuser configuration as the diffuser with straight leading edge and non-axisymmetric end walls but with its passage depth increased by 2.5 times
3. same diffuser configuration as the diffuser with parabolic leading edge and parallel end walls but with its passage depth increased by 2.5 times
4. same diffuser configuration as the diffuser with parabolic leading edge and non-axisymmetric end walls but with its passage depth increased by 2.5 times

Pressure distribution

Figure 6-36 and figure 6-37 show the pressure distribution at midspan of the straight leading edge diffusers. The pressure fields look similar. This is because the midspan is far away from the end wall and the end wall contouring effect is not being felt here. However, it has been observed that pressure is higher in the throat region in the non-axisymmetric

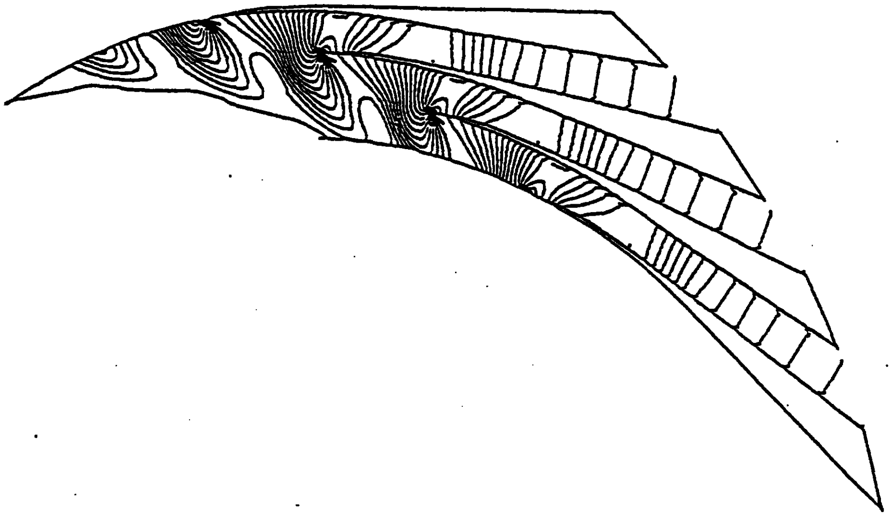

Figure 6-36: Pressure distribution at midspan of the diffuser with straight leading edge, parallel end walls and larger passage depth

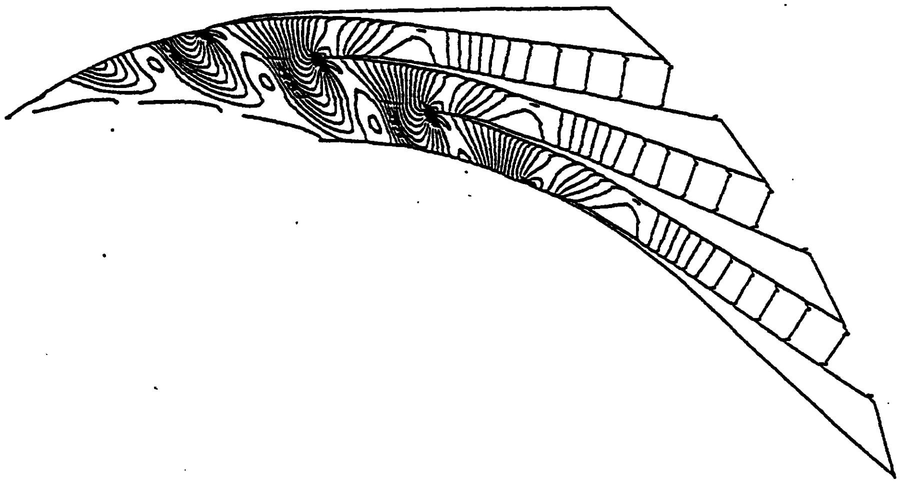

Figure 6-37: Pressure distribution at midspan of the diffuser with straight leading edge, non-axisymmetric end walls and larger passage depth

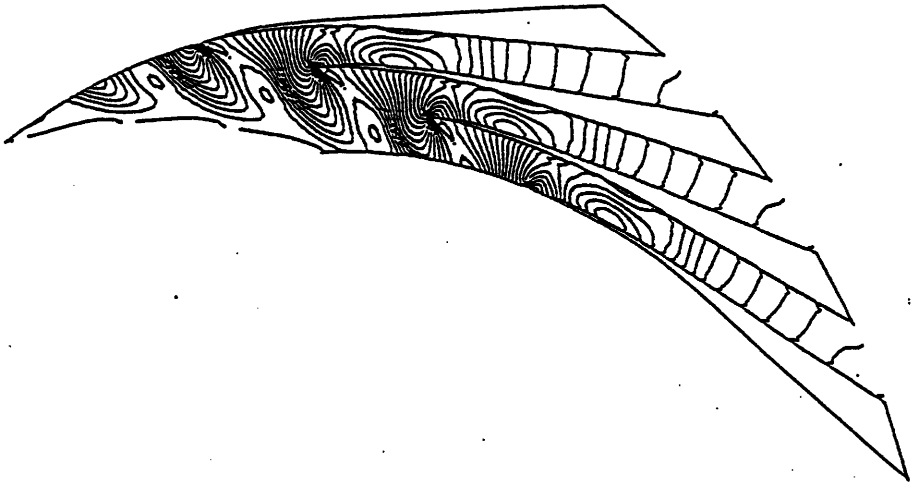

Figure 6-38: Pressure distribution at hub of the diffuser with straight leading edge, non-axisymmetric end walls and larger passage depth

end wall diffuser than that in the parallel end wall one by about 2%. Figure 6-38 shows the pressure distribution of the straight leading edge non-axisymmetric end walls diffuser at hub. It can be seen that in the throat region, the pressure field is different from that in the midspan and from that in the parallel end wall diffuser. Figure 6-39 and figure 6-40 show the pressure distribution at hub of the parabolic leading edge diffusers. Similar comment can be applied to these computed results. The convergence of the pressure side passage height near the throat leads to a local low pressure region around there, hence a higher pressure recovery in that region as will be shown in the next section.

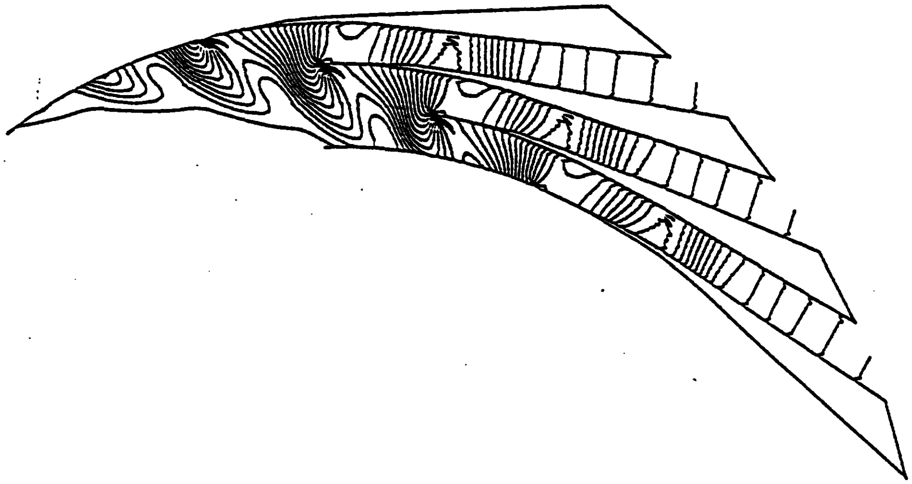

Figure 6-39: Pressure distribution at hub of the diffuser with parabolic leading edge, parallel end walls and larger passage depth

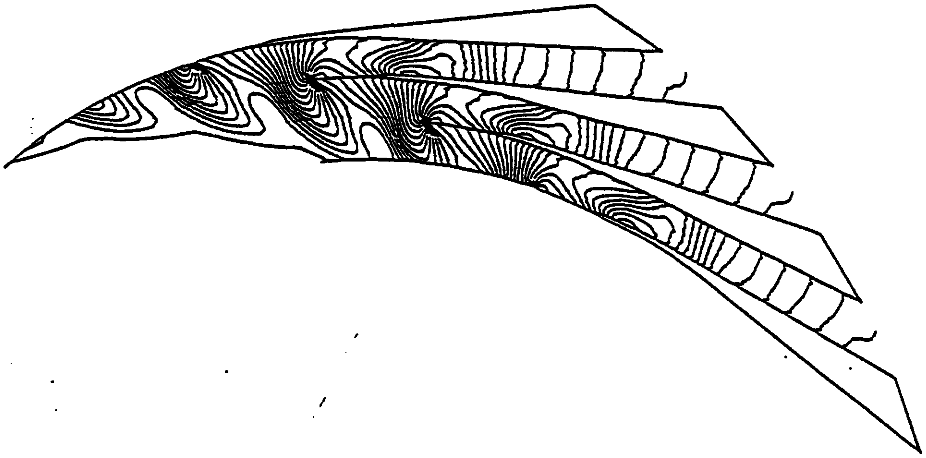

Figure 6-40: Pressure distribution at hub of the diffuser with parabolic leading edge, non-axisymmetric end walls and larger passage depth

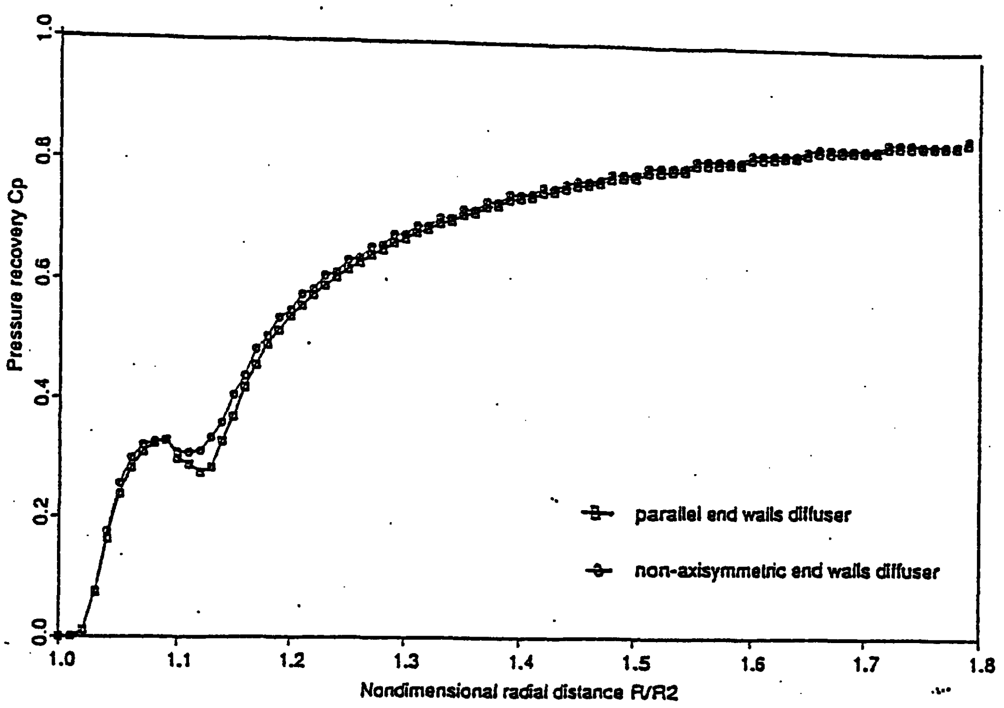

Figure 6-41: Pressure recovery of the diffuser with straight leading edge and larger passage depth

Pressure recovery

It has been shown that increases in the ratio of passage depth to chord length tends to make the effect of contouring end walls more prominent. Figure 6-41 and figure 6-42 show the pressure recovery along the radial direction of different cases. Comparing with figure 6-17 and 6-30, a larger difference can be seen, especially in the throat region. The c_{pD} of the Campbell diffusers are higher than the two dimensional diffusers by 0.05 in both the straight and the parabolic leading edge cases. For these situations, it may be possible that the end wall contouring suggested by Campbell can lead to an improvement in the diffuser performance.

When the ratio of passage depth to chord ratio is increased, the influence of the end wall contouring appears to become more pronounced.

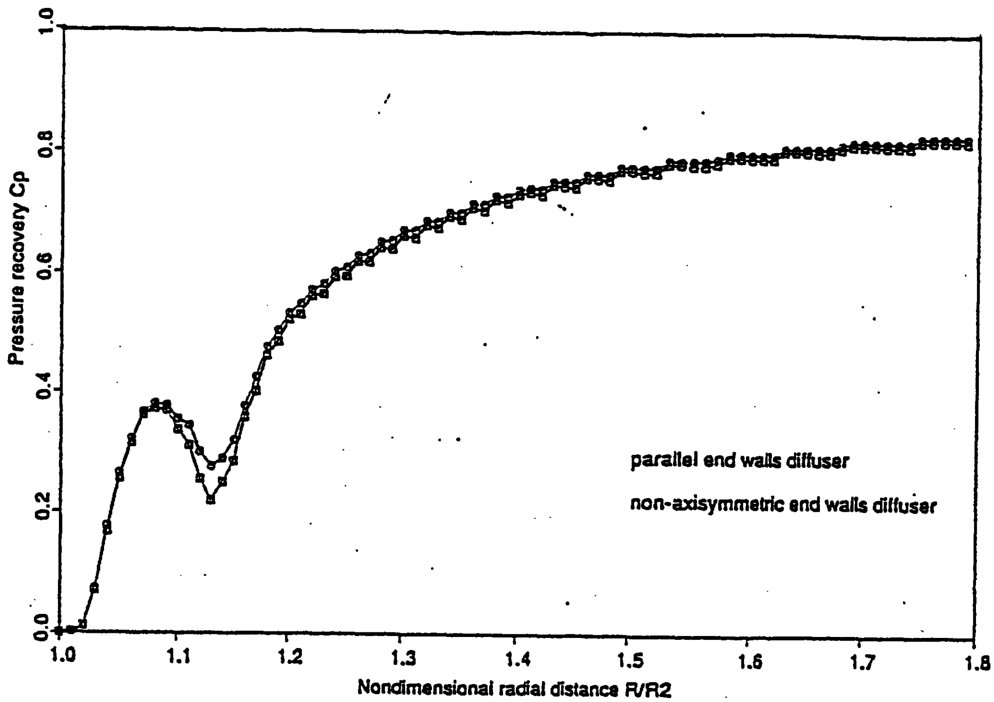

Figure 6-42: Pressure recovery of the diffuser with parabolic leading edge and larger passage depth

Stagnation pressure loss

The mass average stagnation pressure of the straight leading edge diffusers is shown in figure 6-43 and that of the parabolic leading edge diffusers is shown in figure 6-44. Again the stagnation pressure loss is larger for the non-axisymmetric end walls diffusers. The difference in stagnation pressure loss between the parallel end walls cases and the non-axisymmetric end walls cases has increased from 0.2% to 0.5% as the passage depth is increased by 2.5 times. The increase in the difference in stagnation pressure may be numerical since we increase the number of grid points by 2.5 times in the calculation.

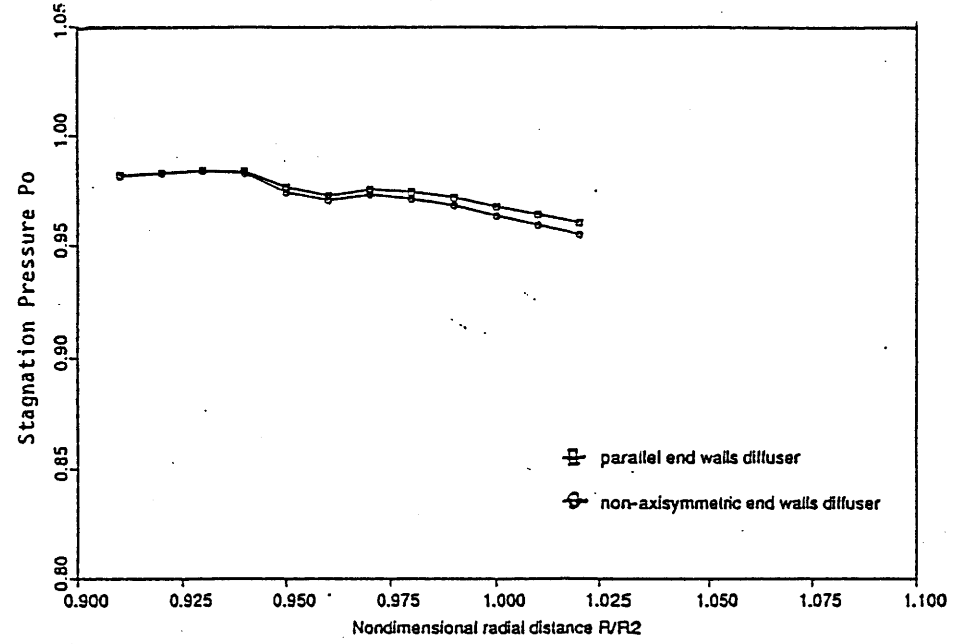

Figure 6-43: Mass average stagnation pressure of diffusers with straight leading edge and larger passage depth

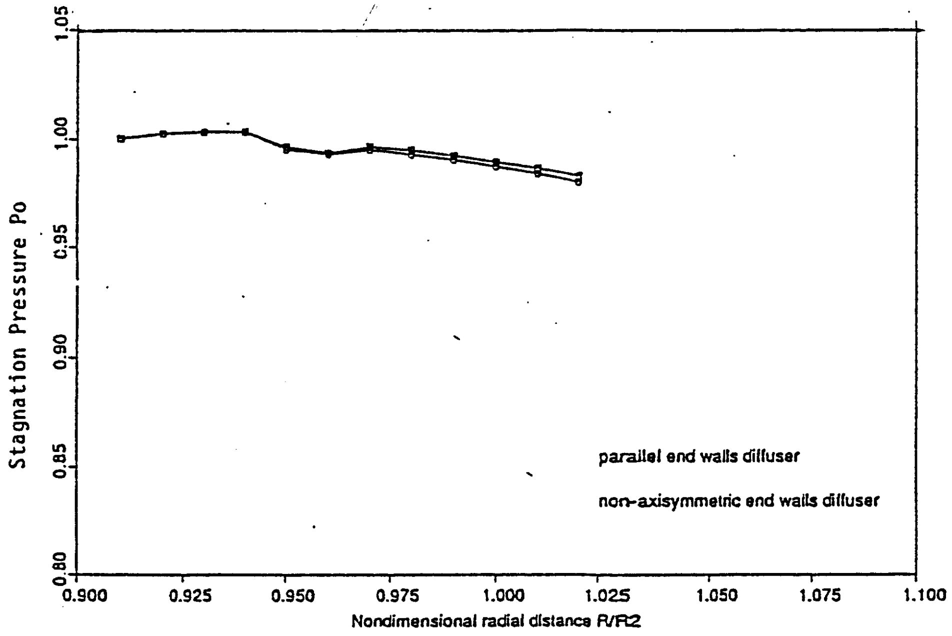

Figure 6-44: Mass average stagnation pressure of diffusers with parabolic leading edge and larger passage depth

6.6.2 The influence of the pitch-chord ratio

In the following investigation, the pitch-chord ratio is changed by changing the stagger angle and the number of blades. The following calculations have been carried out:

1. diffuser with straight leading edge and parallel end walls in which stagger angle has been changed from 71 deg. to 37 deg.
2. diffuser with straight leading edge and non-axisymmetric end walls in which stagger angle has been changed from 71 deg. to 37 deg.
3. same as 1 but with the number of blades increased to 41
4. same as 2 but with the number of blades increased to 41

Pressure distribution

Figures 6-45 and 6-46 show the pressure distribution at end wall of the parallel end walls diffuser (1) and that of the non-axisymmetric end wall diffuser (2). In the throat region of the latter, it has a very similar pressure field as that of the diffuser in previous section. We conclude that this region of low pressure is due to the contouring of end walls and that this effect becomes significant only when either the pitch or the passage depth is comparable to the chord length. Figure 6-47 and 6-48 show the pressure distribution at end wall of 3 and 4. It can be seen that the difference between two pressure fields is diminished when the pitch-chord ratio is lowered by increasing the number of blades.

As mentioned earlier, the investigation is extended for elucidating the influence of the pitch-to-chord ratio on the one-dimensionality of the flow. It is not intended to assess the performance of a diffuser with such a configuration. From this investigation, we see that the end wall contouring has larger effect with larger pitch-to-chord ratio.

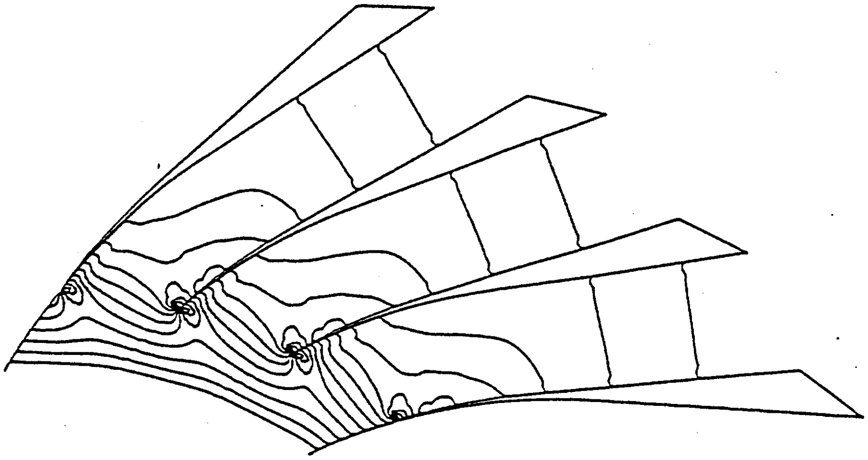

Figure 6-45: Pressure distribution at end wall of the diffuser with straight leading edge, parallel end walls, a smaller stagger angle and 31 blades

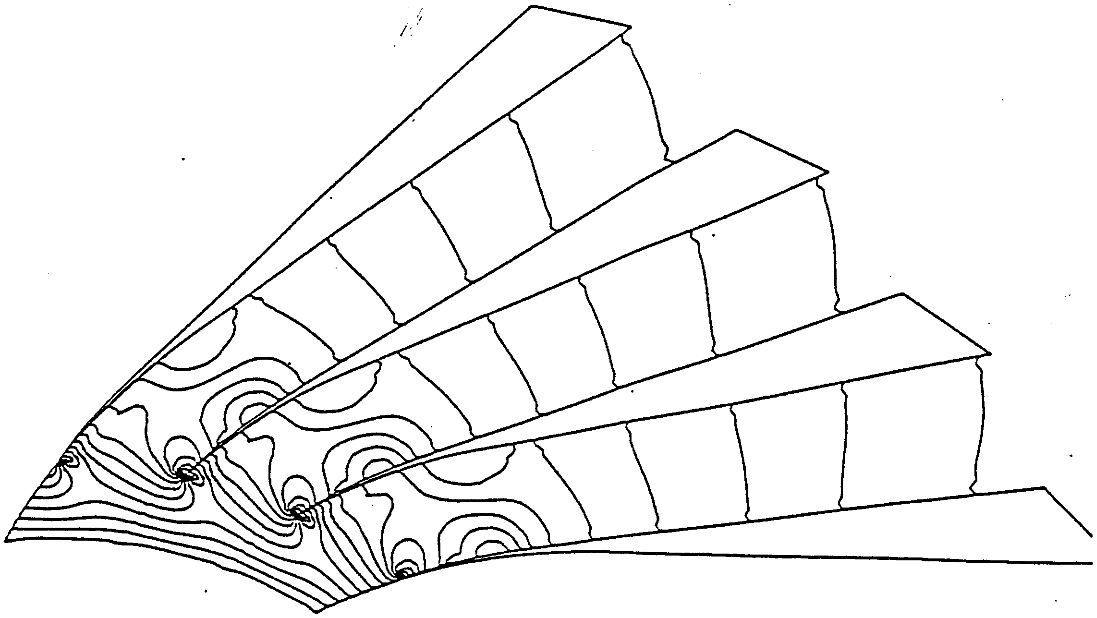

Figure 6-46: Pressure distribution at end wall of the diffuser with straight leading edge, non-axisymmetric end walls, a smaller stagger angle and 31 blades

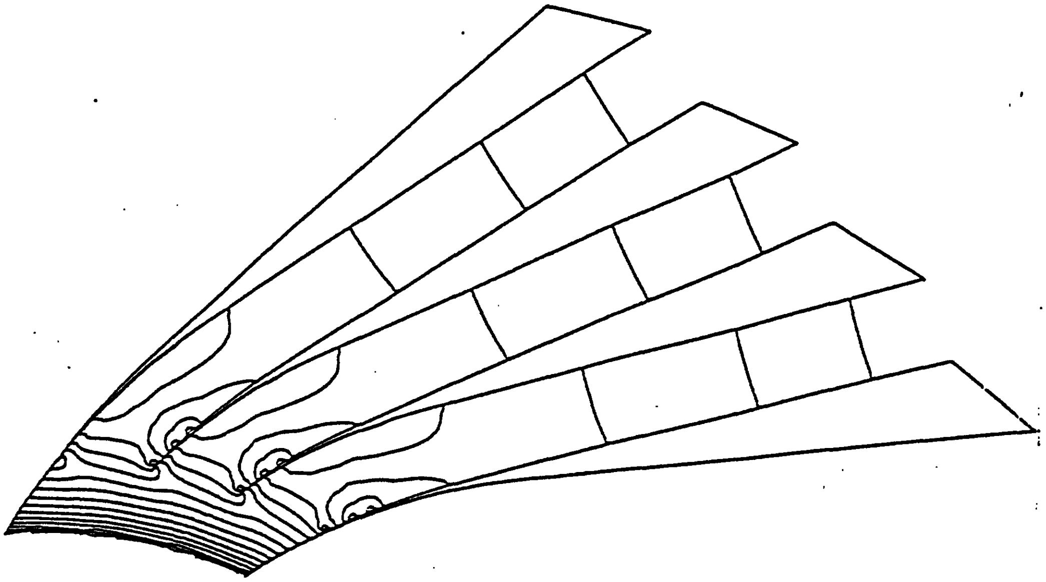

Figure 6-47: Pressure distribution at end wall of the diffuser with straight leading edge, parallel end walls, a smaller stagger angle and 41 blades

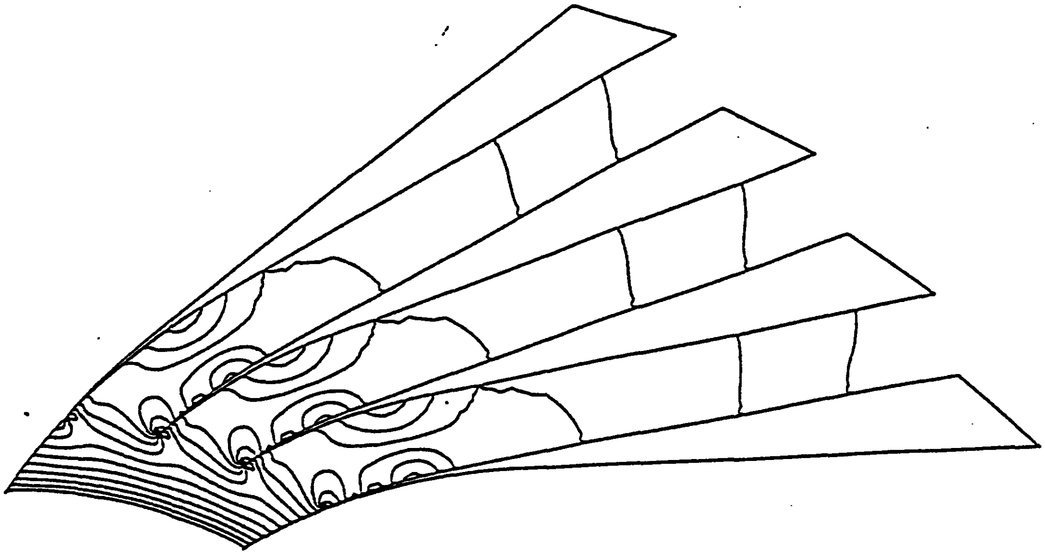

Figure 6-48: Pressure distribution at end wall of the diffuser with straight leading edge, non-axisymmetric end walls, a smaller stagger angle and 41 blades

Chapter 7

Analysis

7.1 Introduction

In this chapter we shall attempt to develop an analysis with the aim of explaining the observed trend in the computational results. Since the validity of the one dimensional flow depends on the configuration of the diffuser and not on the fluid property, incompressible flow model (for its simplicity) can be used to illustrate why the flow is not responsive to geometrical change in the proposed diffuser configuration for investigation. Based on this incompressible flow model, the influence of both the pitch to chord ratio and the passage depth to chord ratio can be assessed. An analysis is also attempted with the intent of explaining the fact that the flow in the proposed diffuser configuration is insensitive to geometrical changes even in transonic regime as one might have anticipated otherwise.

7.2 Incompressible flow analysis

The governing equations expressed in cylindrical co-ordinates are as following:

$$\frac{1}{r}\frac{\partial r v_r}{\partial r} + \frac{1}{r}\frac{\partial v_\theta}{\partial \theta} + \frac{\partial v_z}{\partial z} = 0 \tag{7.1}$$

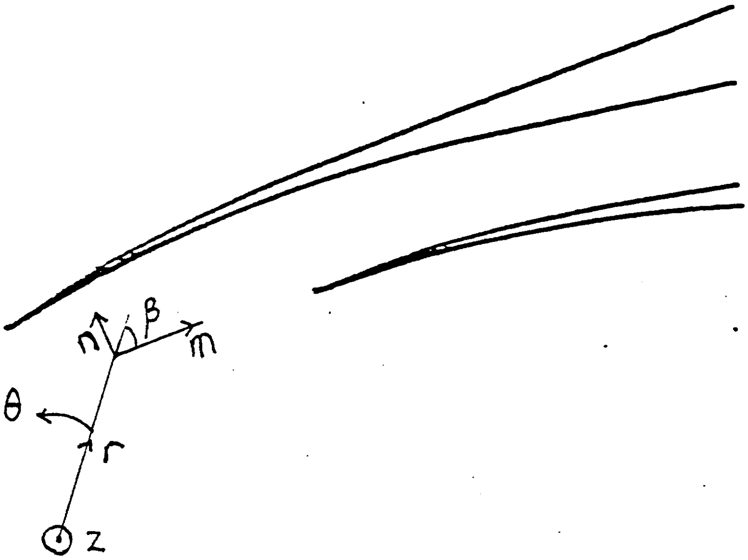

Figure 7-1: The intrinsic coordinate system in $r-\theta$ plane

$$v_r\frac{\partial v_r}{\partial r}+\frac{v_\theta}{r}\frac{\partial v_r}{\partial \theta}+v_z\frac{\partial v_r}{\partial z}-\frac{v_\theta^2}{r}=-\frac{1}{\rho}\frac{\partial P}{\partial r} \tag{7.2}$$

$$v_r\frac{\partial v_\theta}{\partial r}+\frac{v_\theta}{r}\frac{\partial v_\theta}{\partial \theta}+v_z\frac{\partial v_\theta}{\partial z}+\frac{v_r v_\theta}{r}=-\frac{1}{r\rho}\frac{\partial P}{\partial \theta} \tag{7.3}$$

$$v_r\frac{\partial v_z}{\partial r}+\frac{v_\theta}{r}\frac{\partial v_z}{\partial \theta}+v_z\frac{\partial v_z}{\partial z}=-\frac{1}{\rho}\frac{\partial P}{\partial z} \tag{7.4}$$

Let m denote the meridional direction on the $r-\theta$ plane, n the perpendicular to m and β the angle between m and the radial direction. The coordinate system is as shown in fig. 7-1. The meridional velocity is given by

$$v_m=\sqrt{v_r^2+v_\theta^2}$$

It can further be shown that:

$$\begin{aligned} \frac{\partial}{\partial m} &= \cos\beta\frac{\partial}{\partial r}+\frac{\sin\beta}{r}\frac{\partial}{\partial\theta} \\ \frac{\partial}{\partial n} &= -\sin\beta\frac{\partial}{\partial r}+\frac{\cos\beta}{r}\frac{\partial}{\partial\theta} \end{aligned} \tag{7.5}$$

Using (7.5), (7.1) can be rewritten as

$$\frac{v_m\cos\beta}{r}+v_m\frac{\partial\beta}{\partial n}+\frac{\partial v_m}{\partial m}+\frac{\partial v_z}{\partial z}=0 \tag{7.6}$$

Upon multiplying (7.2) by $\cos\beta$,(7.3) by $\sin\beta$, and adding, we arrive at

$$v_m\frac{\partial v_m}{\partial m}+v_z\frac{\partial v_m}{\partial z}=-\frac{1}{\rho}\frac{\partial P}{\partial m} \tag{7.7}$$

Likewise, upon multiplying (7.2) by $\cos\beta$,(7.3) by $\cos\beta$ and subtracting the former from latter, we have

$$v_m^2\frac{\partial\beta}{\partial m}+\sin\beta\frac{v_m^2}{r}+v_zv_m\frac{\partial\beta}{\partial z}=-\frac{1}{\rho}\frac{\partial P}{\partial n} \tag{7.8}$$

so that eqn.(7.4) reduces to

$$v_m\frac{\partial v_z}{\partial m}+v_z\frac{\partial v_z}{\partial z}=-\frac{1}{\rho}\frac{\partial P}{\partial z} \tag{7.9}$$

The flow variables can be made nondimensional based on the following characteristics quantities: they are the velocity at inlet v_∞, chord length c, pitch δ, passage depth ϵ, stagnation pressure at inlet P_0 and density ρ. Three length scales are used in the nondimensionalization because they are needed to characteristize the diffuser configuration. The variables are nondimensionalized to be of order unity as follow:

$$v_m^*=\frac{v_m}{v_\infty};r^*=\frac{r}{c};m^*=\frac{m}{c}$$

$$n^*=\frac{n}{\epsilon};z^*=\frac{z}{\delta};P^*=\frac{P-P_0}{\rho v_\infty^2}$$

We nondimensionalize v_z by v_∞ and then an attempt is made to estimate its order of magnitude from the continuity equation. We have

$$v_z^* = \frac{v_z}{v_\infty}$$

From (7.6),

$$\frac{v_\infty v_m^* \cos\beta}{cr^*} + \frac{v_\infty u_m^*}{\epsilon}\frac{\partial\beta}{\partial n^*} + \frac{v_\infty}{c}\frac{\partial v_m^*}{\partial m^*} + \frac{v_\infty}{\delta}\frac{\partial v_z^*}{\partial z^*} = 0$$

which upon simplifying gives

$$\frac{v_m^* \cos\beta}{r^*} + \frac{u_m^*}{\epsilon/c}\frac{\partial\beta}{\partial n^*} + \frac{\partial v_m^*}{\partial m^*} + \frac{c}{\delta}\frac{\partial v_z^*}{\partial z^*} = 0 \qquad (7.10)$$

From the diffuser configuration we have $\epsilon/c \ll 1$,$\delta/c \ll 1$ and the change of swirl angle across a narrow diffuser passage is negligible so that $\partial\beta/\partial n^* \approx 0$. The first and the third terms of the equation, namely $v_m^* \cos\beta/r^*$ and $\partial v_m^*/\partial m^*$, are of the order unity; hence the last term is almost of order unity,

$$\frac{c}{\delta}\frac{\partial v_z^*}{\partial z^*} = O(1)$$

so that we arrive at

$$v_z^* = O\left(\frac{\delta}{c}\right)$$

It is more convenient to redefine the nondimensional v_z^* to be of order unity for later analysis. From now on, v_z is nondimensionalized by v_∞, c and δ as follows:

$$v_z^* = \frac{c}{\delta}\frac{v_z}{v_\infty}$$

Using this new v_z^*, eqn.(7.10) can be rewritten as

$$\frac{v_m^* \cos\beta}{r^*} + \frac{u_m^*}{\epsilon/c}\frac{\partial\beta}{\partial n^*} + \frac{\partial v_m^*}{\partial m^*} + \frac{\partial v_z^*}{\partial z^*} = 0 \tag{7.11}$$

with $\partial\beta/\partial n^* \approx 0$.

Substituting the nondimensional variables into eqn.(7.7), we have

$$v_m^* \frac{\partial v_m^*}{\partial m^*} + v_z^* \frac{\partial v_m^*}{\partial z^*} = -\frac{\partial P^*}{\partial m^*} \tag{7.12}$$

Likewise from eqn.(7.8)

$$\left(\frac{\epsilon}{c}\right) v_m^{2*} \frac{\partial\beta}{\partial m^*} + \left(\frac{\epsilon}{c}\right) \frac{v_m^{2*}\sin\beta}{r^*} + \left(\frac{\epsilon}{c}\right) u_z^* u_m^* \frac{\partial\beta}{\partial z^*} = -\frac{\partial P^*}{\partial n^*} \tag{7.13}$$

And from eqn.(7.9)

$$\left(\frac{\delta}{c}\right)^2 u_m^* \frac{\partial u_z^*}{\partial m^*} + \left(\frac{\delta}{c}\right)^2 u_z^* \frac{\partial u_z^*}{\partial z^*} = -\frac{\partial P^*}{\partial z^*} \tag{7.14}$$

In eqn.(7.12), we deduce that

$$\frac{\partial P^*}{\partial m^*} = O(1)$$

and from eqn.(7.13), we have

$$\frac{\partial P^*}{\partial n^*} = O\left(\frac{\epsilon}{c}\right)$$

and similarly for eqn.(7.14), we have

$$\frac{\partial P^*}{\partial z^*} = O\left(\left(\frac{\delta}{c}\right)^2\right)$$

This implies that the flow is essential one dimensional when ϵ/c and $\delta/c \ll 1$. In the original four cases with the small passage depth, the flow does not respond to the changes in end wall contouring. When the passage depth is increased, the effect of contouring end wall becomes significant. When the stagger angle is decreased, the flow area is opened up. The pitch-chord ratio ϵ/c is increased. It affects the $\partial P^*/\partial z^*$ term through equation 7.11.

When ϵ/c increases, a larger change in streamline curvature can be sustained across the passage and the term $\partial\beta/\partial n^*$ is no longer negligible. The order of v_z cannot be determined by method of dominant balance since we do not know the relative importance of each term. From the numerical investigation presented in previous chapter, it is found that the flow becomes more responsive to geometrical changes when the pitch-chord ratio increases. Physically, the diffuser passage can be viewed as a thin, narrow and long channel. Changing the passage depth locally does not have much influence on the entire flow field because a substantial pressure gradient between the end walls cannot be developed in a short distance. Therefore, the flow is essentially one-dimensional in this channel.

7.3 Compressible flow analysis

In the previous section, we have used incompressible flow model to show that due to the geometrical constraints, the flow in the proposed diffuser configuration is essentially one dimensional. The flow is in transonic regime in the present investigation. One would anticipate a more drastic change of flow field in response to geometrical changes in transonic flow. In this section, a compressible flow analysis is presented in an attempt to show why the flow is not responsive to geometrical changes even in transonic regime.

It is more convenient to do the following analysis in vector form. The Euler equations can be expressed in three-dimensional intrinsic coordinates [35]. The intrinsic variables are ds and $d\vec{n}$, where ds is the distance along a streamline and $d\vec{n}$ is a two dimensional vector normal to the streamline. The operator ∇ is defined as

$$\nabla = \vec{e_1}\frac{\partial}{\partial n_1} + \vec{e_2}\frac{\partial}{\partial n_2}$$

where the $\vec{e}_i$ are unit vectors orthogonal to each other and to the streamline directions, and $\partial/\partial n_i$ are the intrinsic spatial derivatives in those directions.

The velocity vector in the three dimensional space is expressed as

$$\vec{u} = u\vec{t}$$

$\vec{t}$ is unit vector having the direction of the streamline.

The continuity equation may be written as

$$\frac{\partial \rho u}{\partial s} + \rho u \nabla \cdot \vec{t} = 0 \tag{7.15}$$

and momentum equation in streamline direction is

$$\rho u \frac{\partial u}{\partial s} + \frac{\partial P}{\partial s} = 0 \tag{7.16}$$

Condition of constant entropy along a streamline yields

$$\frac{\partial S}{\partial s} = 0 \tag{7.17}$$

Eqns.(7.15), (7.16) and (7.17) can be used to derive

$$\frac{M^2 - 1}{\rho u^2} \frac{\partial P}{\partial s} + \nabla \cdot \vec{t} = 0 \tag{7.18}$$

$\nabla \cdot \vec{t}$ may be interpreted as the logarithmic derivative $\partial A/(A\partial s)$ of the area of the streamtube. The other form of (7.18) may be more familiar

$$\frac{\partial P}{\partial s} + \frac{\rho u^2}{M^2 - 1} \frac{\partial A}{A \partial s} = 0 \tag{7.19}$$

The momentum equations in the normal directions are in the form of

$$\rho u^2 \frac{\partial \vec{t}}{\partial s} + \nabla P = 0 \tag{7.20}$$

It can be seen in equation (7.19) that the area change $\partial A/\partial s$ is amplified by a factor of $1/(M^2 - 1)$ in the transonic regime. However, the Campbell diffuser end walls are tailored in such a way that the area distribution along the flow direction is the same as that in the diffuser with parallel end walls, i.e. $\partial A/\partial s$ is the same in both cases; thus $\partial P/\partial s$ is expected to be similar. From equation (7.20), we see that $\partial \vec{t}/\partial s$ is a function of the streamline pattern and there is no explicit Mach number dependence in this equation, therefore the pressure gradients in the crossflow directions (∇P) should not change significantly in the transonic regime. This simple analysis serve as a mean to illustrate that Campbell Diffuser concept is not quite effective even in the transonic flow regime.

Chapter 8

Summary and conclusion

8.1 Summary

The Campbell diffuser concept has been assessed using four diffuser configurations. Careful study of the computed results in chapter 6 and the analysis in the previous chapter appears to indicate that two parameters are of particular importance, namely the pitch-to-chord ratio and the passage depth to chord ratio. If these two ratios are small, the flow is essentially one dimensional. That is, the flow will not respond to changes in end wall contouring, as long as the one dimensional area distribution is unchanged. This is true even in the transonic regime because the transonic effect influences the flow field through the area change in streamwise direction and such area change is the same in the Campbell diffusers and the corresponding parallel end wall diffusers.

Bow shocks appear in the semi-vaneless region from the computed results. It is observed that contouring the end walls in the channel region has little effect on the shocks. However, since the present investigation uses the inviscid flow model, the computed results may not represent a realistic shock structure in the flow.

Based on the present computational result, it appears that there is a gain of 5% in c_{pD} in Campbell diffusers when the pitch chord ratio or passage depth-chord ratio is sufficiently large. The stagnation pressure loss and entropy generation are functions of shock strength and are hardly affected by end wall contouring.

8.2 Conclusion

1. For the four proposed configurations, Campbell effect is negligible as shown in the computed results.
2. Two important parameters control the nature of the flow. They are the pitch-to-chord ratio and the passage depth to chord ratio. When they are small, the flow is essentially one-dimensional.

Bibliography

[1] R.C. Dean and L.R. Young. The fluid dynamic design of advanced centrifugal compressors, Aug 1976. Prsented at the Fluid Dynamics Institute, Hanover, NH.

[2] R. C. Dean. the fluid dynamic design of advanced centrifugal compressor. Technical report, Creare Science and technology, 1974.

[3] D.P. Kenny. Supersonic radial diffusers. In *Lecture Series on Advanced Compressors*, 39. AGARD, 1970.

[4] Y. Senoo and Y. Kinoshita. Influence of inlet flow conditions and geometries of centrifugal vaneless diffusers on critical flow angle for reverse flow. *Journal of Fluids Engineering*, 1977.

[5] Y. Kinoshita Y. Senno and M. Ishida. Asymmetric flow in vaneless diffusers of centrifugal blowers. *Journal of Fluids Engineering*, 1977.

[6] S. Baghdadi and A.T. McDonald. Performance of three vaned radial diffusers with swirling transonic flow. *Journal of Fluids Engineering*, June 1975.

[7] M.A. Rayan and T.T. Yang. An investigation of vane-island diffusers at high swirl. *ASME*, 1980.

[8] M. Inoue and N.A. Cumpsty. Experimental study of centrifugal impeller discharge flow in vaneless and vaned diffusers. *Jouranl of Engineering for Gas Turbine and Power*, 1984.

[9] I. Teipel. the influence of different geometries for a vaned diffuser on the pressure distribution in a centrifugal compressor. *ASME*, 1984.

[10] I. Teipel and A. Wiedermann. Three-dimensional flowfield calculation of high-loaded centrifugal compressor diffusers. *Journal of Enginnering for Gas Turbine and Power*, 1987.

[11] H.O. Jeske and I. Teipel. A theoretical investigation of transonic flow in radial compressor diffusers. *ASME*, 1982.

[12] S. Colantuoni et al. Optimisation of transonic flow radial vaned diffuser. In *Transonic and Supersonic Flow Phenomenon*, 1985.

[13] K. Campbell. Us patent no. 4099891, 1978.

[14] A. Wennerrstorm. Private communication.

[15] C. Osborne. turbocharger compressor design and development. Technical report, Creare Science and technology, July 1979.

[16] D. Japikse. *Centrifugal Compressor Design and Performance.* Concepts ETI Inc., 8th edition, 1986.

[17] C.J. Sagi and J.P. Johnson. The design and performance of two dimensional, curved diffusers. *ASME*, 1967.

[18] J.D. Denton. the calculation of fully three dimensional flow through any type of turbomachine blade row. In *3-D computation techniques applied to internal flows in propulsion systems.* AGARD, 1985.

[19] M. L. Celestina, R. A. Mulac, and J. J. Adamczyk. A numerical simulation of the inviscid flow through a counterrotating propeller. *ASME*, June 1986.

[20] A. Jameson, W. Schmodt, and E. Turkel. numerical solutions of euler equations by finite volume methods using runge kutta time stepping schemes. *AIAA*, June 1981.

[21] D. G. Holmes and S. S. Tong. a three dimensional euler solver for turbomachinert blade rows. *ASME*, 107, 1985.

[22] A. Rizzi. Numerical implementation of solid body boundary conditions for the euler equations. *ZAMM*, 58, 1978.

[23] T.W. Roberts. *Euler Equation Computations For the Flow Over a Hovering Helicopter Rotor.* PhD thesis, MIT, 1986.

[24] J.D. Denton. An improved time marching method for turbomachinery flow calculation. *ASME*, 1982.

[25] J. F. Thompson, F.C. Thames, and C. W. Mastin. a code for numerical generation of boundary-fiited curvilinear coordinate systems on fields containing any number of arbitrary two-dimensional bodies. *journal of computational physics*, 1977.

[26] J. F. Thompson, F.C. Thames, and C. W. Mastin. automatic numerical generation of boundary-fiited curvilinear coordinate systems on fields containing any number of arbitrary two-dimensional bodies. *journal of computational physics*, 1974.

[27] J. F. Thompson, F. C. Thames, and C. W. Mastin. boundary-fitted curvilinear coordinate systems for solution of partial differential equations on fields containing any number of arbitrary two-dimensional bodies. Contractor report 2729, NASA, 1976.

[28] L. Liu. Private communication.

[29] L. Howarth, editor. *Modern developments in fluid dynamics : High speed flow*, chapter 5. Oxford University Press, 1957.

[30] H. Lichtfuss and H. Starken. supersonic casecade flow. In Kuchemann, editor, *progress in aerospace science*, volume 15. Pergamon Press, 1974.

[31] R. Courant and K. O. Friedrichs. Supersonic flow and shock waves. In *Pure and Applied Mathematics*, volume 1. Interscience, 1948.

[32] F.X. Dolan and P.W. Runstadler Jr. Design, development and test of laser velocimeter for a small 8:1 pressure ration centrifugal compressor. Contractor Report 134781, NASA, March 1979.

[33] D. Jakipse and C. Osborne. Optimization of industrial centrifugal compressors. *ASME*, 1986.

[34] N.A. Cumpsty. Private commumication.

[35] W.D. Hayes and R.F. Prostein. *Hypersonic Flow Theory.* Academic Press, 1966.